REVIEW

Check for updates

Research progress of Mn-based low-temperature SCR denitrification catalysts

Jiadong Zhang,[ab] Zengyi Ma, (ID) *[ab] Ang Cao, (ID) [a] Jianhua Yan,[ab] Yuelan Wang,[c] Miao Yu,[d] Linlin Hu[d] and Shaojing Pan[d]

Selective catalytic reduction (SCR) is a efficiently nitrogen oxides removal technology from stationary source flue gases. Catalysts are key component in the technology, but currently face problems including poor low-temperature activity, narrow temperature windows, low selectivity, and susceptibility to water passivation and sulphur dioxide poisoning. To develop high-efficiency low-temperature denitrification activity catalyst, manganese-based catalysts have become a focal point of research globally for low-temperature SCR denitrification catalysts. This article investigates the denitrification efficiency of unsupported manganese-based catalysts, exploring the influence of oxidation valence, preparation method, crystallinity, crystal form, and morphology structure. It examines the catalytic performance of binary and multicomponent unsupported manganese-based catalysts, focusing on the use of transition metals and rare earth metals to modify manganese oxide. Furthermore, the synergistic effect of supported manganese-based catalysts is studied, considering metal oxides, molecular sieves, carbon materials, and other materials (composite carriers and inorganic non-metallic minerals) as supports. The reaction mechanism of low-temperature denitrification by manganese-based catalysts and the mechanism of sulphur dioxide/water poisoning are analysed in detail, and the development of practical and efficient manganese-based catalysts is considered.

aState Key Laboratory of Clean Energy Utilization, Zhejiang University, Hangzhou, 310027, China. E-mail: mazy@zju.edu.cn; Tel: +86 0571 87952822

bInstitute for Carbon Neutrality, Ningbo Innovation Center, Zhejiang University, Ningbo, 315100, China

cShenyang Environmental Resources Exchange, Shenyang 110000, China

dXizi Clean Energy Equipment Manufacturing Co., Ltd, Hangzhou, 311500, China

1 Introduction

Nitrogen oxides (NO_X), including nitric oxide (NO), nitrogen dioxide (NO_2) and nitrous oxide (N_2O), are significant air pollutants. They contribute to ecological and environmental problems such as acid rain, ozone depletion, and photochemical smog. Furthermore, NO_X can cause respiratory illnesses and pose a risk to human health.[1–3] NO_X emissions originate from both stationary and mobile sources. Stationary sources include

Jiadong Zhang is a graduate student. He will start his master's degree in 2022 and his doctoral degree in 2024. He is studying at Zhejiang University, majoring in energy and power engineering. His research direction is the preparation and application of low-temperature SCR denitrification catalysts.

Jiadong Zhang

Zengyi Ma is a professor at the School of Energy Engineering, Zhejiang University, and received his PhD in Engineering from Zhejiang University in 1998. His main research direction is clean waste incineration technology, and he has recently been engaged in the research of clean incineration technology of hazardous waste rotary kilns, clean incineration technology of high-fluorine and high-chlorine hazardous wastes, and waste incineration fly ash resource technology.

Zengyi Ma

coal-, oil-, and gas-fired boilers and industrial furnaces, as well as waste gas pollution from petrochemical, metallurgical, and building material production processes. These emissions are typically released through exhaust stacks. Mobile sources include emissions from motor vehicles, ships and aircrafts. For thermal power plants, fossil fuel-fired industrial boilers and domestic boilers, the technologies for controlling NO_X emissions encompass both combustion process control and post-combustion control. Combustion control technologies, also known as low-NO_X combustion technologies, primarily include the use of low-NO_X burners, staged combustion, and flue gas recirculation.[4]

To control NO_X emissions, post-combustion control technologies are frequently employed.[5] These include selective catalytic reduction (SCR) and selective non-catalytic reduction (SNCR), amongst others.[6] SCR technology involves the reaction of NH_3, urea, H_2 or CO with NO_X on the surface of catalyst to produce N_2 and H_2O.[7] It offers advantages such as high denitrification efficiency, good product selectivity, and relatively mature technological base.[8,9] The performance of the catalyst is crucial, directly impacting the denitrification effectiveness of the SCR system.[10] Traditionally, SCR systems have widely utilised vanadium and tungsten-based catalysts on a TiO_2 support for medium- to high-temperature applications (300–400 °C). However, these catalysts have drawbacks, including a narrow high-temperature activity window, potential for V_2O_5 sublimation at high temperatures, and biotoxicity concerns.[11] Furthermore, SCR reactors are typically installed upstream of flue gas purification equipment, such as dust collectors and desulphurisation units. As the flue gas is not yet purified, the catalyst must withstand high dust concentrations, as well as the poisoning effects of SO_2 and H_2O. These factors can deactivate the catalyst, reducing denitrification efficiency and service life, leading to increased operating costs due to catalyst replacement.[12] Placing the SCR reactor in a lower temperature region, such as after the flue gas purification processes and devices for dust removal and desulphurisation, could mitigate the negative impact of dust, SO_2, and H_2O on the catalyst. This could extend catalyst service life and reduce operating costs.[13] Consequently, developing catalysts with activity in a lower temperature window holds significant practical value.

In recent years, the development and research of low-temperature catalysts has become a prominent area of focus within the field of SCR. Zeolites modified with noble metal catalysts (Pt, Pd, Ag) and transition metal ions (Cu, Fe) have been extensively investigated. Transition metal oxide catalysts (Mn, Co, Ni, Fe, Cu, *etc.*) exhibit excellent redox properties and promising low-temperature catalytic activity due to their facile electron gain and loss from their d-orbitals. These catalysts have emerged as a hot topic in the research of low-temperature NH_3-SCR catalysts. Manganese oxides, with their abundant of multivalent states (such as Mn^{4+}, Mn^{3+}, Mn^{2+}) possess strong redox capabilities, leading to excellent low-temperature denitrification activity and product (N_2) selectivity. This makes them a promising candidate for industrial applications and they are considered to be the transition metal oxide catalysts with the best low-temperature SCR catalytic activity.[14-17] This article reviews unsupported manganese-based catalysts, including single, binary/multicomponent manganese-based catalysts, and supported manganese-based catalysts. Supported catalysts are
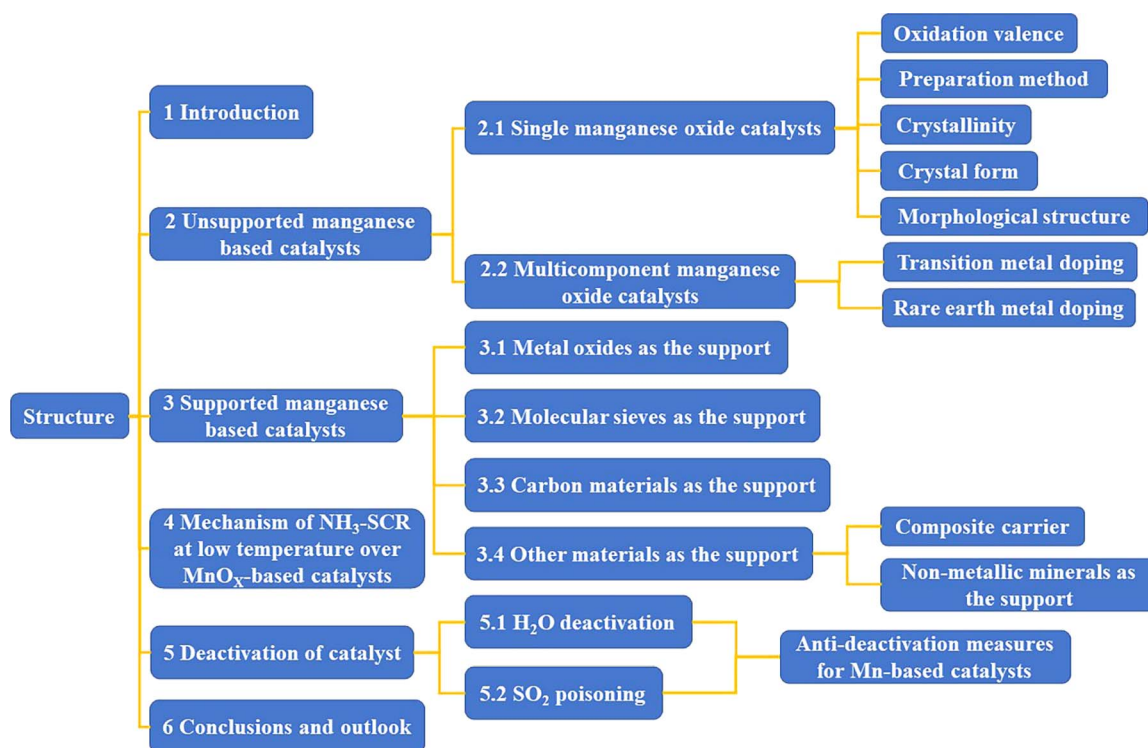
Fig. 1 The structure of article.

explored using metal oxides, molecular sieves, carbon materials, and other materials (composite carriers and inorganic non-metallic minerals) as supports. The reaction mechanisms of low-temperature denitrification using manganese-based catalysts, as well as the mechanism of SO_2/H_2O poisoning, are analysed and explored. The development of manganese-based catalysts with high catalytic activity, good product selectivity, and stability at low temperatures is envisioned. The structure of the article is shown in Fig. 1.

2   Unsupported manganese-based catalysts

2.1   Single manganese-based catalysts

Mn has attracted extensive attention due to its abundant oxidation valence states and corresponding metal oxides, such as Mn^{4+}, Mn^{3+}, Mn^{2+}.[18] These different valence states contribute to its excellent redox properties.[19,20] In addition, the catalytic activity of MnO_X is also affected by the crystallinity, crystal crystalline structure and morphological structure.[21] For example, Huang et al.[22] investigated the relationship between different valence states of industrially pure MnO_X compounds (MnO_2, Mn_2O_3, Mn_3O_4 and MnO) under the conditions of $[NO] = [NH_3] = 500$ ppm, $[O_2] = 3$ vol%, N_2 as the balanced gas, and GHSV = 27 000 h^{-1}. The NO_X conversion in the range of 120–250 °C was 100% for pure MnO_2 and the NO_X conversion of pure Mn_2O_3 reached a maximum of 92% at 160 °C. The NO_X conversion of pure MnO_X catalysts in the range of 50–150 °C followed the order: MnO_2 > Mn_2O_3 > Mn_3O_4 > MnO.[23,24] Yang et al.[25] prepared manganese oxides with different valence states (MnO_2, Mn_2O_3, and Mn_3O_4) by redox hydrothermal method. They conducted qualitative and quantitative investigations on the denitrification activity, NO_2 generation, N_2 selectivity and N_2O generation (reaction condition: $[NO_X] = [NH_3] = 500$ ppm, $[O_2] = 11$ vol%, N_2 as the balanced gas and GHSV = 36 000 h^{-1}). Within the temperature range of 75–150 °C, the catalyst denitrification activity of different valence manganese oxides, the generation of NO_2, and the generation of N_2O increased with the increase of the temperature. However, the selectivity of N_2 was in the opposite trend, decreasing as the temperature increased. The catalyst SCR of MnO_2 generated more N_2O, and the catalysts of Mn_2O_3 and Mn_3O_4 had better N_2 selectivity than MnO_2. Liu et al.[26] found that due to the high oxygen instability of Mn_2O_3, resulting in high N_2 selectivity of Mn_2O_3 in SCR reaction, Mn_2O_3 is more active than Mn_3O_4 for direct catalytic decomposition of NO and N_2O. Kapteijn et al.[15] prepared different valence states of MnO_X, and the activity per unit of surface area was in the order of MnO_2, Mn_5O_8, Mn_2O_3, Mn_3O_4 and MnO, which showed a decreasing trend in the activity per unit surface area with decreasing Mn valence, resulting in the different valence states of MnO_X exhibiting different efficiencies in removing NO_X ($[NO] = 500$ ppm, $[NH_3] = 550$ ppm, $[O_2] = 2$ vol%, He as the balanced gas, $T = 112$–302 °C and flow rate = 50 cm^3 (STP) min^{-1}). MnO_2 showed the best efficiency in removing NO, and Mn_2O_3 showed the best selectivity of the product (N_2). Tang et al.[27] prepared β-MnO_2 and α-Mn_2O_3 by

redox-hydrothermal method to study the performance of NH_3-SCR denitrification at 150 °C ($[NO] = [NH_3] = 680$ ppm, $[O_2] = 3$ vol%, He as the balanced gas and GHSV = 90 000 ml g^{-1} h^{-1}). MnO_2 with a high valence state had higher a NO conversion and N_2O generation rate than Mn_2O_3. MnO_2 had a higher activation ability to NH_3 molecules, which could break more N–H bonds in NH_3 molecules, give more adsorbed nitrogen atoms, and react with gaseous NO to generate more N_2O. The above studies have shown from different perspectives that different valence states of Mn lead to different NO_X removal performance and product (N_2) selectivity. In general, the denitrification performance of pure MnO_X catalysts decreases with the decrease of the Mn valence state. Mn^{4+} has the highest NO_X removal efficiency and poor product (N_2) selectivity due to its strong oxidizing ability, whereas Mn^{3+} has excellent NO_X removal efficiency and the best product (N_2) selectivity due to its oxidation ability second only to Mn^{4+}. The various unstable oxygen and oxidation valence states of MnO_X are necessary for MnO_X catalysts to complete the redox catalytic cycle.[28]

Differences in the preparation methods of MnO_X catalysts also affect the low-temperature denitrification activity of the catalysts. Tang et al.[16] prepared amorphous unsupported manganese-oxide catalysts using three methods and investigated the catalytic activity of NH_3-SCR denitrification under oxygen-rich and low-temperature conditions. They concluded that the activity of amorphous catalysts decreased in the order of MnO_X (co-precipitation method), MnO_X (low-temperature solid-phase reaction method), and MnO_X (rheological phase reaction method) in the low-temperature range of 50–80 °C ($[NO] = [NH_3] = 500$ ppm, $[O_2] = 3$ vol%, N_2 as the balanced gas and GHSV = 47 000 h^{-1}). Meanwhile, Tang et al.[16] prepared MnO_X catalysts by the low-temperature solid-phase reaction method, and examined the effects of calcination at different temperatures: 350 °C, 450 °C, 550 °C, and 650 °C. It was concluded that the crystallinity of catalysts prepared by the low-temperature solid-phase reaction method decreased with the decrease of the calcination temperature, but the catalytic activity was opposite that. The lower the crystallinity of the catalyst, the more favourable the amorphous phase is for the insertion and release of protons and promotes the chemical adsorption/desorption and redox reaction of the bulk or surface of the catalyst particles.[29,30] That coincides with Andreoli et al.[31] finding that catalysts with low crystallinity have better catalytic performance than crystalline catalysts. To clarify the effect of MnO_X crystal crystalline structure on the denitrification efficiency of SCR reaction, Gong et al.[32] prepared four different nanocrystalline structures of α-, β-, δ- and γ-MnO_2, and the scanning electron microscope (SEM) images are shown in Fig. 2. The NO_X redox efficiency of different crystal structures was compared as γ-MnO_2 > α-MnO_2 > δ-MnO_2 > β-MnO_2. γ-MnO_2 and α-MnO_2 have stronger reducing ability and stronger acidic centre, and more chemisorbed oxygen exists on the surface. In addition, the γ-MnO_2 catalysts show alternating single and double bonds, which are easy to collapse and produce a large number of point-space defects and vacancies. There are more reduction/oxidation active sites in the catalyst, and γ-MnO_2 has the highest catalytic activity. Experiments showed that NO_X

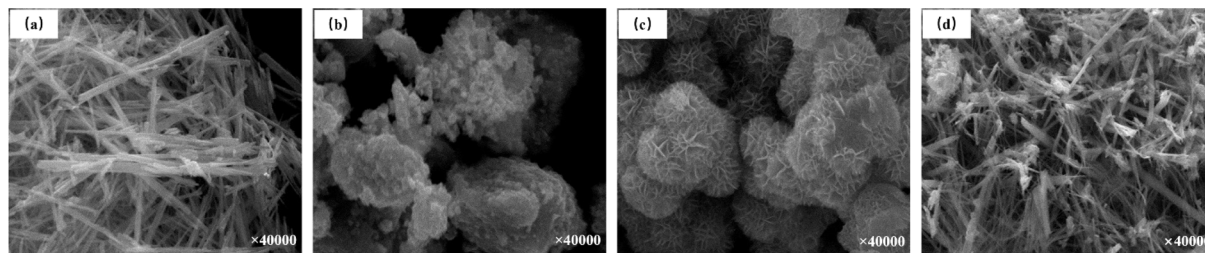Fig. 2 The SEM images of four different MnO_2 nanocrystals: (a) α-MnO_2; (b) β-MnO_2; (c) δ-MnO_2; (d) γ-MnO_2 (reprinted from ref. 32. Copyright 2017, with permission from Elsevier).

conversion reached 90% using γ-MnO_2 catalyst in the temperature range of 140–200 °C ([NO] = 720 ppm, [NH_3] = 800 ppm, [O_2] = 3 vol%, N_2 as balanced gas, and GHSV = 30 000 h^{-1}). Meanwhile, Zhao et al.[33] investigated the oxidation performance of pure MnO_2 catalysts concerning the crystalline structure of NO_X for the most active MnO_2 and found that its oxidation ability was consistent with the results of Gong et al.[32]

The morphological structure of MnO_X is also another factor affecting the denitrification activity of the catalysts. Yu et al.[34] synthesized α-Mn_2O_3 nanocrystalline catalysts with three morphologies: octahedron (α-Mn_2O_3-O), truncated octahedral bipyramid (α-Mn_2O_3-TOB), and hexagonal nanosheets (α-Mn_2O_3-HN) by hydrothermal method. The influence of the crystal surface effect of α-Mn_2O_3 catalyst on its catalytic activity was investigated. The results showed that the exposure of the crystalline surface of the α-Mn_2O_3-HN catalysts {001} increased the surface density of the reactive oxygen species and enhanced the low-temperature reduction of Mn^{4+}. Tian et al.[35] prepared catalysts with different morphologies of MnO_2 nanotubes, nanorods and nanoparticles by hydrothermal method. The scanning electron microscope (SEM) images are shown in Fig. 3. The results showed that the nanorod-shaped MnO_2 catalysts exhibited the best denitrification performance at low temperatures (100–300 °C) and 36 000 h^{-1} GHSV, which was mainly attributed to the low crystallinity of the nanorods, the high lattice oxygen content, the strong reducing ability and a large number of strong acid centres.

Therefore, the performance and product (N_2) selectivity of pure MnO_X catalysts for NO_X removal are not only related to the

oxidation valence state of the Mn, but also closely related to the preparation method, crystallinity, crystal lattice surface, and morphological structure as well, as shown in Fig. 4.

These factors affecting the catalytic activity of MnO_X are interactive and interrelated. MnO_X nanorods have lower crystallinity than MnO_X nanotubes. In-depth studies are needed to determine whether the morphology or the crystallinity is the dominant factor leading to the excellent SCR catalytic activity of MnO_X nanorods. While morphology, crystallinity, and specific surface area are physical properties of catalysts, chemical properties such as oxidation valence and lattice oxygen content are more indicative of the nature of catalyst performance. A single MnO_X catalyst exhibits excellent low-temperature denitrification performance, but the poor stability of MnO_X catalysts, resistance to H_2O passivation, susceptibility to SO_2 and alkali metal poisoning, and poor selectivity of the product (N_2) affect its practical engineering applications.[36,37] Therefore, mixing other metal oxides with MnO_X for modification or doping is an important way to solve these problems.

2.2 Binary/multicomponent composite manganese-based catalysts

The introduction of other metal oxides into MnO_X catalysts to form binary or multi-component composite manganese-based catalysts with the help of doping and modification can improve the reaction performance of single-component MnO_X catalysts. Many researchers have introduced transition metals and rare earth metals into Mn-based catalysts for doping and
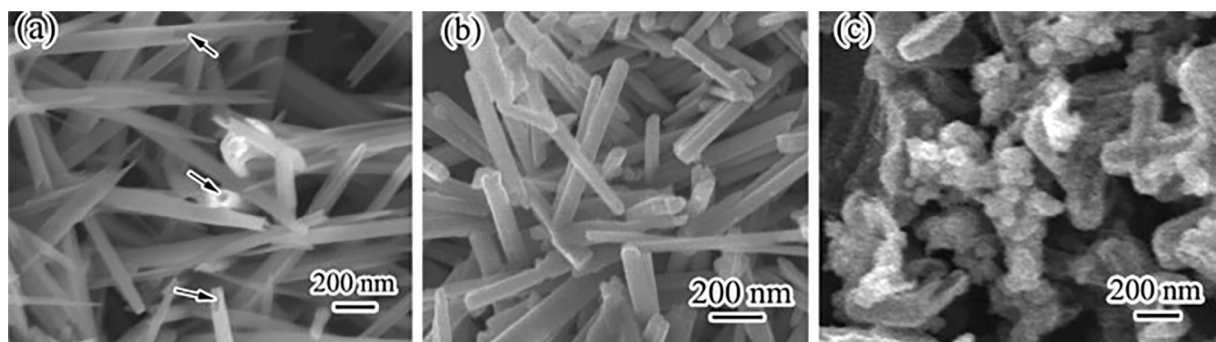

Fig. 3 The SEM images of the MnO_2 catalysts (a) nanotubes; (b) nanorods; (c) nanoparticles (reprinted from ref. 35. Copyright 2011, with permission from Elsevier).
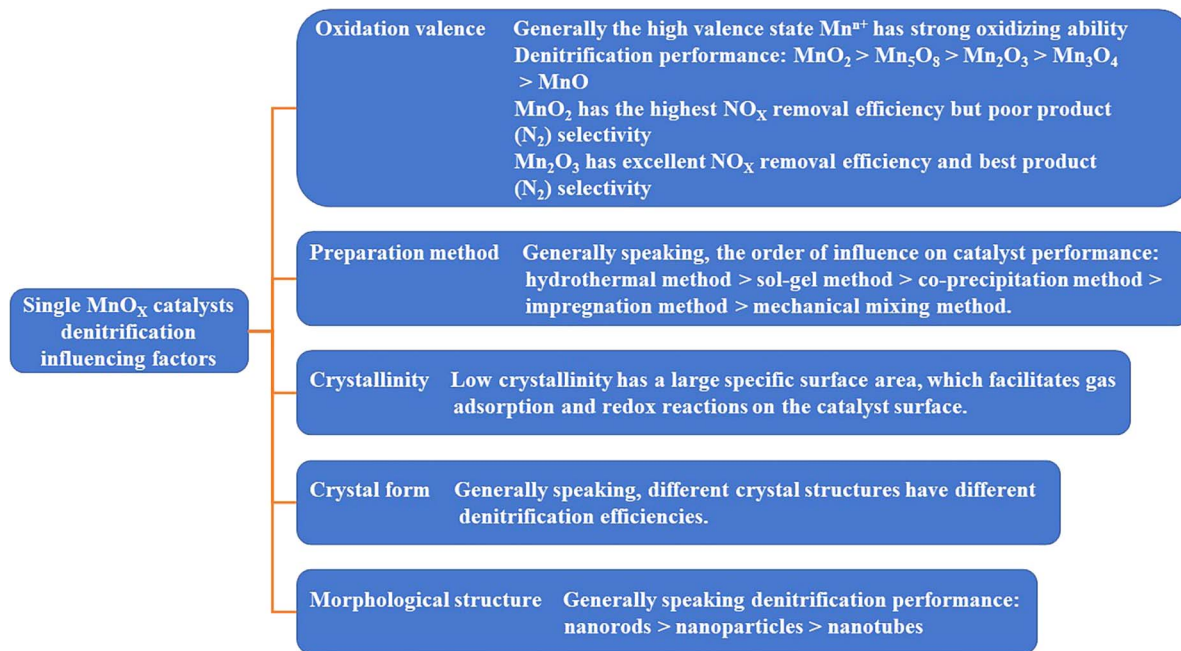
Fig. 4 Factors affecting the catalytic activity of single MnO_X catalysts.

modification, such as Ti,[38] Fe,[39,40] Cu,[41] Ce,[42,43] Sm,[44] Co,[45] *etc.*, see Table 1.

Doping transition metals can be used as structural additives to optimize the catalyst structure and enhance the stability of the catalyst, thus improving the low-temperature denitrification activity and SO_2 resistance of Mn-based catalysts. Fe and Cu are often added to denitrification catalysts as additives, which resulted in a significant increase in the N_2 selectivity of the SCR catalysts.[46,47] Zhang *et al.*[48] prepared Fe–Mn nanostructured oxide catalysts with NO_X conversion rates exceeding 90% over the 130–300 °C range ([NO] = [NH$_3$] = 1000 ppm, [O$_2$] = 3 vol%, N_2 as balanced gas, and GHSV = 72 000 h^{-1}), while N_2 selectivity was significantly improved compared to single MnO_X catalysts. The doping of FeO_X made the interaction between Mn^{n+} and Fe^{n+} ions stronger, which improved the denitrification ability of

$FeMnO_X$ catalysts, and consequently improved the low-temperature N_2 selectivity of the catalysts.[49] Li *et al.*[50] synthesized a series of $MnFeO_X$ catalysts with different Fe/Mn molar ratios by using the hydrothermal method and found that $MnFe_{0.1}O_X$ exhibited the highest catalytic performance, with a NO_X removal efficiency close to 100% at 200–350 °C ([NO] = [NH$_3$] = 500 ppm, [O$_2$] = 5 vol%, N_2 as balanced gas, and GHSV = 28 000 h^{-1}). The addition of Fe induced the redox reaction process, increasing the oxygen concentration and acid sites for surface chemical adsorption. Gao *et al.*[51] used the citric acid method for the preparation of Cr–Mn mixed-oxide catalysts, with high specific surface area, a large number of acidic sites and spinel structure, which exhibited excellent SCR denitrification activity with nearly 100% NO_X removal efficiency and good N_2 product selectivity at 100–225 °C. Yan *et al.*[52] prepared

Table 1 Part of transition metal and rare earth metal doped modified manganese based catalysts

Catalysts	Mental doped	Preparation	Reaction conditions		Denitrification efficiency	Ref.
$Mn_{0.3}Ce_{0.3}TiO_X$	Ti, Ce	Sol–gel methode	1000 ppm NH_3, 1000 ppm NO, 3 vol% O_2	GHSV = 40 000 h^{-1}	≈100% (125–350 °C)	**38**
$MnFeO_X$	Fe	Coprecipitation method	500 ppm NH_3, 500 ppm NO, 5 vol% O_2	GHSV = 30 000 h^{-1}	>80% (150–200 °C)	39 and 40
$(Cu_{1.0}Mn_{2.0})_{1-\delta}O_4$	Cu	Coprecipitation method	500 ppm NH_3, 500 ppm NO, 3 vol% O_2	GHSV = 100 000 h^{-1}	>80% (130–240 °C)	**41**
$MnCoCeO_X$	Co, Ce	Self-assembly, impregnation, heat treatment	500 ppm NH_3, 500 ppm NO, 5 vol% O_2	GHSV = 24 000 h^{-1}	≈100% (90–240 °C)	42 and 43
$MnSmO_X$	Sm	Reversed-phase precipitation	500 ppm NH_3, 500 ppm NO, 5 vol% O_2	GHSV = 60 000 h^{-1}	>80% (225–325 °C)	**44**
MnO_2–Co_3O_4–CeO_2	Co, Ce	Coprecipitation method	1000 ppm NH_3, 1000 ppm NO, 5 vol% O_2	GHSV = 70 000 h^{-1}	>90% (150–175 °C)	**45**

a new class of low-temperature NH_3-SCR catalysts with Cu_w-$Mn_yTi_{1-y}O_X$ using layered double hydroxide as the precursor. The $Cu_1Mn_{0.5}Ti_{0.5}O_X$ catalyst achieved up to 90% NO_X conversion at 200 °C ([NO] = [NH_3] = 1000 ppm, [O_2] = 5 vol%, Ar as balanced gas, and flow rate = 200 ml min^{-1}). It was concluded that its excellent catalytic performance was mainly related to the higher specific surface area and surface acidity as well as the higher number of active MnO_2 and CuO species. The catalyst exhibited significant tolerance to SO_2 and H_2O when CuO was introduced. Shi et al.[53] synthesized nanorods, nanorods, and hollow nanotubes with the structure of the $MnCoO_X$ catalysts to investigate their low-temperature denitrification activity and tolerance to SO_2 and H_2O. The formation process is shown in Fig. 5. The results show that the presence of Co and Mn facilitates the improvement of redox properties, which promotes low-temperature catalytic activity, whereas the hollow nanotube-structured MnCo catalysts exhibit excellent SO_2 resistance, with more than 80% NO_X conversion at 150 °C even under the co-presence of H_2O and SO_2 ([NO] = [NH_3] = 2000 ppm, [O_2] = 8 vol%, [H_2O] = 10 vol%, [SO_2] = 200 ppm, N_2 as balanced gas, and GHSV = 90 000 h^{-1}). This superior performance was attributed to the unique hollow nanotube structure, which effectively shielded the active sites on the inner surface from SO_2 and alkali metal poisoning. Zhao et al.[54] prepared CoMn composite oxides with layered morphology by coprecipitation. CoMn-LS-250 calcined at 250 °C showed high activity with up to 91% NO_X conversion at 60 °C and good SO_2 resistance at 300 °C. This was mainly attributed to the special layered structure on the surface of the catalyst, which made it rich in Lewis acid sites and strong redox capacity, as well as the high content of Mn^{4+}, Co^{3+} and surface adsorbed oxygen. All these indicate that the structure of the catalyst has a certain role in the catalytic performance.

Rare earth metal additives, such as Ce,[42] Sm,[44] Nd,[55] Gd,[56] etc., have good SCR denitrification performance due to their excellent oxygen storage, redox properties and good SO_2 resistance. Li et al.[57] prepared MnO_X–CeO_2 hollow binary nanotubes by a template-free method. The SEM images are presented in

Fig. 6. The maximum NO_X conversion was 96% at 100 °C and GHSV = 30 000 h^{-1} with high N_2 selectivity ([NO] = [NH_3] = 1000 ppm, [O_2] = 5 vol%, N_2 as balanced gas, and GHSV = 30 000 h^{-1}). The abundant Mn^{4+} and O_α (surface adsorption of face), uniformly distributed active species of Mn and Ce elements, the large amount of Lewis acid and a high specific surface area brought by the hollow porous structure. The surface acidity is closely related to the activity of the catalysts,[58] more acidic centres are conducive to the improvement of NH_3 adsorption and low-temperature activity of the catalyst. The incorporation of Ce and the hollow porous structure reduces the possibility of SO_2 occupying the surface active centres, and the doping of Ce prevents the formation of ammonium sulfate salts from blocking the active centres, thus showing good SO_2 resistance. Li et al.[59] prepared CeO_2–MnO_X catalysts with core–shell structure by chemical precipitation method. Due to the high crystallinity of α-MnO_2 as well as high concentrations of Mn^{4+} and Ce^{3+}, the catalyst exhibited relatively high NO conversion in the range of 110–220 °C at a molar ratio of CeO_2/MnO_X = 0.6. Furthermore, it demonstrated good resistance to SO_2 and H_2O at an air velocity of 40 000 h^{-1}, [NO] = [NH_3] = 800 ppm, [O_2] = 5 vol%, [SO_2] = 100 ppm, [H_2O] = 10 vol%, Ar as balanced gas.

In addition to the $CeMnO_X$ binary catalyst, a third metal oxide was doped into the $CeMnO_X$ binary catalyst in the hope of further improving its reaction performance. Chang et al.[60] investigated the denitrification performance of Cr, In, W, Ge, Sn, and Fe-doped $CeMnO_X$, and found that the Sn-doped catalyst was modified to significantly increase the concentration of oxygen vacancies on the surface of the catalyst, improve the surface acidity and favoured the oxidation of NO to NO_2. The NO_X conversion rate exceeds 97% at 80 °C. Ren et al.[61] investigated the performance of γ-Fe_2O_3 and Ce/Mn doped catalysts by quantum chemistry and density functional theory and found that SO_2 and SO_3 preferred to adsorb on the Ce sites, exposing more Fe active sites to participate in the NH_3-SCR reaction, whereas Mn doping had little effect on the adsorption. Hao et al.[62] prepared a monolithic Mn–Fe–Ce–Al–O low-temperature
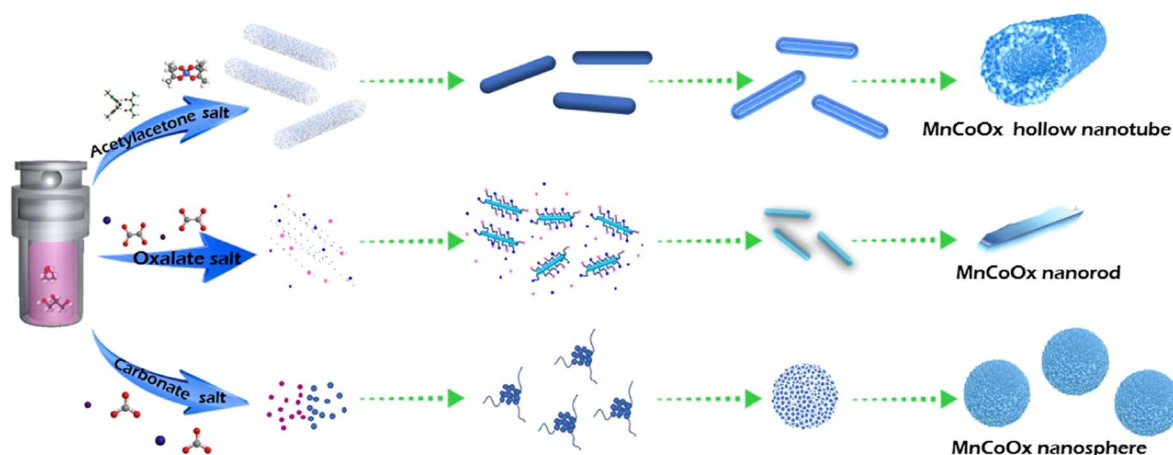

Fig. 5 The schematic illustration of the formation of the hollow nanotube, nanorod, and nanosphere of $MnCoO_X$ oxides (eeprinted from ref. 53. Copyright 2021, with permission from Elsevier).
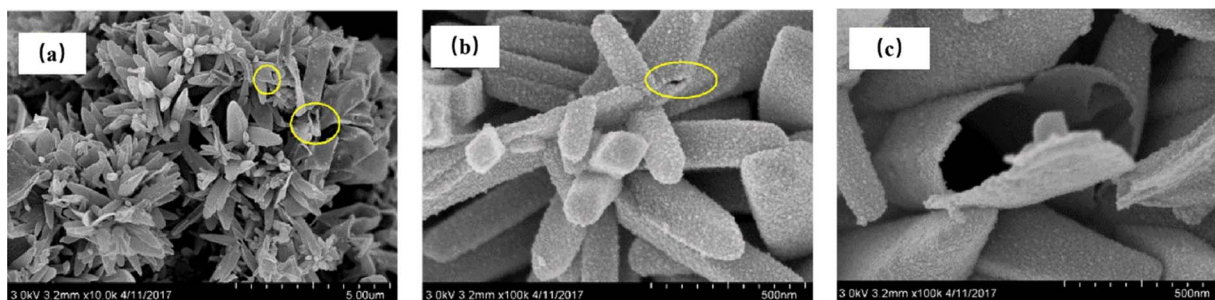
Fig. 6 The SEM images of MnO_X–CeO_2 hollow nanotube: (a–c). (Reprinted from ref. 57. Copyright 2018, with permission from Elsevier).

denitrification catalyst, which had more than 80% NO conversion in the absence of SO_2 and H_2O at a reaction temperature of 100 °C; the NO conversion could be maintained at about 70% at 100 °C and SO_2 concentration of 200 ppm, showing excellent SO_2 resistance (reaction condition: $[NO] = [NH_3] = 200$ ppm, air balance and GHSV = 1667 h^{-1}). Characterization analysis revealed that the presence of Ce can preferentially react with SO_2 to avoid the formation of manganese sulfate, while the presence of Ce increases the amount of chemically adsorbed oxygen on the surface of the catalyst. The addition of Ce and Fe species helps to improve the catalyst's resistance to SO_2 and H_2O.

In summary, the doped metal oxide modification enhanced the synergistic effect between metal ions, increased the number of surface oxygen vacancies and active sites, making the active components on the catalyst surface dispersed to a higher degree, and strengthened the degree of mutual migration between electrons, thereby accelerating the NH_3-SCR denitrification reaction. Manganese-based catalysts were modified by doping with one or more metal elements to improve the denitrification efficiency, and product selectivity (N_2), broaden the activity temperature window, and increase the resistance to H_2O and SO_2.[63]

3   Supported manganese-based catalysts

The carrier plays an important role for low-temperature SCR catalysts,[64] and the appropriate carrier is conducive to the improvement of the activity of SCR catalysts.[65] Compared to unsupported catalysts, supported catalysts can not only promote the dispersion of the active components on its surface due to high specific surface area, thus preventing the catalyst from agglomeration and sintering of larger particles, but also provide more active sites for the active components dispersed on the carrier. This strengthens the synergistic effect between the active components and carrier, thereby improves the catalytic activity,[66] product (N_2) selectivity and anti-poisoning resistance.[67–69] In the following, the performance of supported Mn-based catalysts will be investigated in terms of metal oxides, molecular sieves, carbon materials and other materials (composite carriers and inorganic non-metallic minerals) as carriers.

3.1   Metal oxide as the support

Al_2O_3 and TiO_2 (ref. 70) as typical metal oxides, have been widely used as supports for MnO_X.[71] Yao et al.[72] prepared MnO_X/SiO_2, MnO_X/Al_2O_3, MnO_X/TiO_2 and MnO_X/CeO_2 catalysts, noting that the specific surface area of MnO_X/WO_y (W=Si, Al, Ti, and Ce) catalysts follows the order MnO_X/SiO_2 > MnO_X/γ-Al_2O_3 > MnO_X/ TiO_2 > MnO_X/CeO_2 (see Fig. 7). However, in the simulated conditions: $[NO] = [NH_3] = 500$ ppm, $[O_2] = 5$ vol%, N_2 as balanced gas and GHSV = 60 000 h^{-1}, it was found that MnO_X/ Al_2O_3 had the best performance of all the current catalysts, which was mainly related to its good dispersibility, the high number of reducing acidic sites, strong NO_X adsorption capacity and abundant Mn^{4+} content. Liu et al.[73] prepared Mn-based catalysts with γ-Al_2O_3, TiO_2 and MCM-41 as carriers by impregnation method, and investigated their catalytic oxidation performance for NO at low temperatures ($T = 80$–200 °C, $[NO] = 500$ ppm, $[O_2] = 5$ vol%, GHSV = 24 000 h^{-1}). The results showed that Mn/γ-Al_2O_3 with good Mn dispersion, excellent redox properties, moderate amount of Mn^{3+}, Mn^{4+} and abundant chemically adsorbed oxygen, as well as the interaction between Mn and γ-Al_2O_3 carriers resulted in the strongest NO adsorption performance of Mn/γ-Al_2O_3, which led to its optimal catalytic activity. TiO_2 can interact with active catalytic components to produce
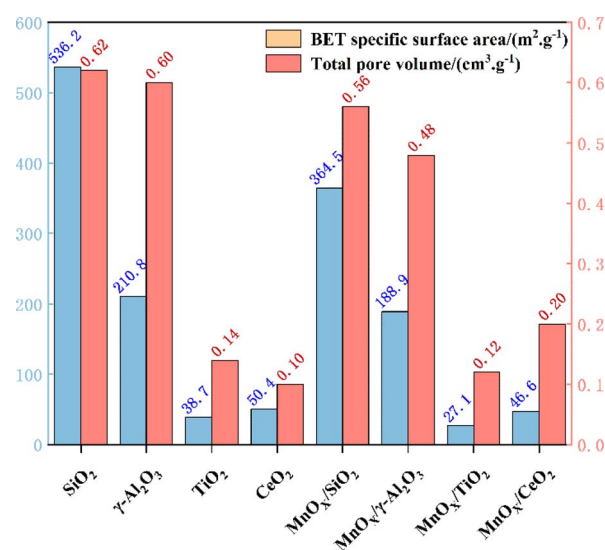

Fig. 7   BET data of different carriers and MnO_X/WO_y catalysts.

a synergistic effect and enhance catalytic activity, so it is often used as a carrier for various catalysts. Zeng et al.[74] prepared MnO_2/MO_X (Mn/M, M = Al, Si and Ti) catalysts by impregnation method to investigate the performance of NH_3-SCR reaction for NO_X removal from the point of view of the supports' effect on the generation of N_2O, and found that the degree of dispersion of MnO_2 on MnO_2/MnO_X was MnSi > MnAl > MnTi (see Fig. 8). However the TiO_2 support formed a stronger activity–support interaction with the impregnated MnO_2, which produced a synergistic effect, thus MnTi was more strongly active than MnSi and MnAl in reducing MnO_2. The strong activity–support interaction of MnTi induced the transfer of NH_3 activation sites from Mn sites to Ti sites, which resulted in the separation of the activation centres of NH_3 and NO + O_2, and effectively suppressed the over-activation of NH_3. Therefore, the generation of N_2O on MnTi was much smaller than that on MnSi and MnAl, which facilitated the SCR reaction. In addition, TiO_2 possesses different morphologies (anatase, rutile and brookite), and due to the different surface properties, different crystalline facets exhibit different activities. Li et al.[75] employed anatase TiO_2 as a support to prepare a Mn–Ce/TiO_2 catalyst with varying exposed crystal faces, specifically the {001} and {101} facets. Their research revealed that preferential exposure of the anatase TiO_2 {001} crystal facet significantly enhanced the catalyst's SO_2 resistance and N_2 selectivity. This preferential exposure effectively inhibited the formation of ammonium sulphate and ammonium bisulfate, thereby preventing the sulphation of the active Mn and Ce components. This mechanism reduces the poisoning effect of SO_2 on the metal active sites.

CeO_2, as an active support, can form strong interactions with surface-supported components and possess abundant active oxygen to improve redox properties and thus increasing denitrification efficiency.[76] Yao et al.[72] prepared MnO_X catalysts supported on TiO_2, Al_2O_3, TiO_2 and CeO_2, investigating their H_2 consumption and reduction peak temperatures. The study revealed that the H_2 consumption of MnO_X/SiO_2, MnO_X/Al_2O_3, and MnO_X/TiO_2 were broadly similar. Conversely, MnO_X/CeO_2

catalysts exhibited significantly greater H_2 consumption compared to the above three catalysts. The reduction temperature of the MnO_X/CeO_2 catalyst was notably lower than the other three catalysts. From the perspective of the coordination state of Mn species, these can be attributed to the formation of a more unstable triangular biconical coordination structure between Mn and CeO_2 coupled with synergistic effects between Mn and Ce. This structure facilitated the easier removal of capping O^{2-} compared to surface lattice O^{2-} and the subsurface lattice O^{2-}, resulting in the superior reduction performance of MnO_X/CeO_2 catalysts, thereby enhancing their denitrification performance. Li et al.[77] prepared a MnO_X–CeO_2 nanosphere catalyst with excellent low-temperature activity and SO_2 resistance, and found that the MnO_X–CeO_2 nanosphere catalysts had long-time operation stability at 150 °C ([NO] = [NH_3] = 500 ppm, [O_2] = 5 vol%, N_2 as the balanced gas and GHSV = 60 000 h^{-1}). The research showed that good redox properties, grain size small, high specific surface area and abundant surface Ce^{3+}, Mn^{4+} and oxygen species are the main reasons for its excellent catalytic performance.

3.2 Molecular sieve as the support

Molecular sieves with unique pore structures, large specific surface areas, good adsorption, and high hydrothermal stability, such as SAPO-34,[78] ZSM-5,[79] β,[80] zeolite (copper- and iron-zeolites),[81,82] etc., are often used as supports for low-temperature NH_3-SCR catalysts, which is one of the hotspot supports for Mn-based catalysts at present. Lou et al.[83] prepared a series of Mn/ZSM-5 catalysts by the precipitation method and calcined the catalysts at different calcination temperatures. The results showed that MnO_X existed on the catalyst surface in the form of Mn_3O_4 and amorphous MnO_2 when calcined below 500 °C, and when the calcination temperature was 600 °C, the low-activity Mn_2O_3 was formed, and it became the main phase at 700 °C. The Mn concentration and specific surface area on the surface of the catalyst decreased with increasing calcination temperature. The NH_3-SCR catalytic activity tests showed that the Mn/ZSM-5 catalyst calcined at 300 °C exhibited the best NO removal performance with almost 100% NO conversion in the range of 150–390 °C ([NO] = [NH_3] = 600 ppm, [O_2] = 4.5 vol%, N_2 as the balanced gas and GHSV = 36 000 h^{-1}). Li et al.[84] prepared a low-cost fly ash-derived SBA-15 molecular sieve as a support. The Fe–Mn/SBA-15 catalyst was prepared by the impregnation method. In the range of 150–250 °C, Fe–Mn/SBA-15 exhibited higher NH_3-SCR activity, with synergistic effects between Mn and Fe, high dispersion on the surface of the species, suitable Mn^{4+}/Mn^{3+} ratio, and the adsorption of oxygen concentration and low-temperature oxidation activity, which are favourable for the improvement of NH_3-SCR catalytic activity. Xu et al.[80] prepared two series of Mn/β and Mn/ZSM-5 catalysts by impregnation method using manganese nitrate, manganese acetate, and manganese chloride as the three precursors, respectively and investigated the catalytic activity of these catalysts within a reaction temperature window of 50–350 °C. In the range of 220–350 °C, the NO removal rate of Mn/β and Mn/ZSM-5 catalysts prepared by manganese acetate were above 80%, and the Mn/β prepared by manganese acetate
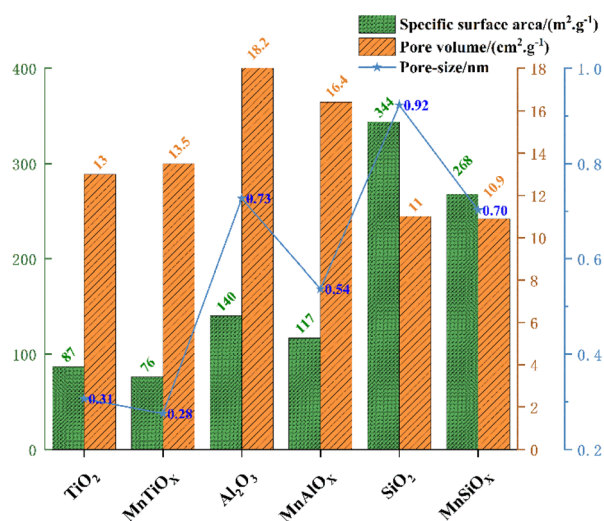

Fig. 8 BET data of different carriers and MnO_2/WO_y catalysts.

exhibited the highest NO conversion—97.5% at 240 °C, and its activity remained above 90% in the 220–350 °C temperature window ([NO] = 1000 ppm, [NH$_3$] = 1100 ppm, [O$_2$] = 5 vol%, N$_2$ as the balanced gas and GHSV = 50 000 h^{-1}). The excellent catalytic performance was attributed to the highly dispersed MnO$_X$ active phase, the appropriate amount of weak acidic centres, the higher concentration of surface Mn species, and more surface unstable oxygen groups.

3.3 Carbon materials as the support

Carbon materials with large specific surface area, porous structure, strong adsorption capacity, and high catalytic efficiency can also be used as Mn-based catalyst supports, such as activated carbon (AC),[85] activated carbon fibre (ACF), graphene (GE), carbon nanotubes (CNTs), and semi-coke.[86] Jiao et al.[87] used a hydrothermal method for the preparation of graphene-supports manganese oxides (MnO$_X$/GR), investigating the effect of different MnO$_X$ loadings on the catalytic activity of low-temperature NH$_3$-SCR It was found that the catalytic activity was optimal at a Mn loading of 20% (wt), and the NO removal efficiency was greater than 90% at 190 °C, and the NO removal efficiency was close to 100% at 220 °C ([NO] = [NH$_3$] = 600 ppm, [O$_2$] = 3 vol%, Ar as the balanced gas and GHSV = 45 000 h^{-1}). The MnO$_X$ was dispersed as nanoparticles on the graphene surface, and it was mainly coexisted with various MnO$_X$ compounds, such as MnO, Mn$_3$O$_4$, and MnO$_2$. The catalyst with a loading of 20% (wt) has high SCR activity. The reason is that it contains high-valent manganese and the surface adsorbed oxygen content increases, the redox ability is strong in the low-temperature zone, and the number of active sites is large. Zhang et al.[88] prepared MnO$_X$/CNTs catalysts with different Mn/C molar ratios by in situ precipitation. It was found that the prepared MnO$_X$/CNTs catalysts had excellent low-temperature SCR activity with NO conversion of 57.4–89.2% for 1.2 (wt%) MnO$_X$/CNTs catalysts in the temperature range of 80–180 °C ([NO] = [NH$_3$] = 500 ppm, [O$_2$] = 5 vol%, N$_2$ as the balanced gas and GHSV = 35 000 h^{-1}). This performance was attributed to the amorphous nature of the MnO$_X$ catalysts, characterised by high Mn^{4+}/Mn^{3+} and O$_S$/(O$_S$ + O$_L$) ratios (O$_S$: surface adsorbed oxygen, O$_L$: lattice oxygen). Yang et al.[89] used the impregnation method to load the transition metals such as Mn, Ce, V and Fe onto nitric acid-modified biomass coke (BC) and tested for low-temperature SCR catalytic activity. The order of NO removal efficiencies in the range of 125–225 °C was Mn/BC > Ce/BC > V/BC > Fe/BC > BC, with the Mn/BC catalyst achieving the highest NO removal efficiency of 87.6% at 200 °C ([NO] = [NH$_3$] = 600 ppm, [O$_2$] = 11 vol%, N$_2$ as the balanced gas and GHSV = 12 000 h^{-1}). This high performance is primarily attributed to the high specific surface area of BC support, the abundant oxygen-containing groups that provide highly active adsorption sites for NH$_3$ and the graphite microcrystalline structure that can act as an oxidant for NO.

3.4 Other materials as the support

Composite carriers and inorganic non-metallic minerals are also often used as substrate materials for SCR reactions.

Composite carriers can give full play to the advantages of different carriers relative to a single carrier, enhance the synergistic effect between active components and carriers, and improve the catalytic activity of the catalyst. He et al.[90] prepared TiO$_2$–CeO$_2$, ZrO$_2$–CeO$_2$ and TiO$_2$–ZrO$_2$–CeO$_2$ supports by the sol–gel method. They found that the low-temperature catalytic activity and SO$_2$ resistance performance of MnO$_X$/TiO$_2$–ZrO$_2$–CeO$_2$ catalysts were significantly better than those of catalysts with other carriers. Additionally, the structural instability of the Mn-based catalysts was improved to reduce the temperature of the crystal formation and suppress the crystal growth. The specific surface area and pore volume of the catalysts were increased to avoid the accumulation of active components due to the high calcination temperature. Qi et al.[91] found that the catalysts on the composite carriers of Al$_2$O$_3$ and TiO$_2$ had better pore structure, better surface dispersion of the active substance carriers, and more active ligand NH$_3$ in the L-acid site, and the best denitrification efficiency than the single carriers such as TiO$_2$ or ZrO$_2$. Li et al.[65] also prepared Mn-Ce/Ti-Al-O composite carrier-type catalysts by impregnation method and found that Ti–Al–O composite carriers have larger specific surface area, pore volume and lower crystallinity than pure TiO$_2$. When the temperature is lower than 150 °C, the Mn–Ce/TiAlO$_X$ catalysts have higher NO conversion than the Mn–Ce/TiO$_2$ catalysts. After the passage of SO$_2$, the NO$_X$ removal rate of the Mn–Ce/TiAlO$_X$ catalyst decreased less than that of the Mn–Ce/TiO$_2$ catalyst, which greatly improved the SO$_2$ resistance. This is primarily due to the improved dispersion of catalyst activity on the Ti–Al–O composite carrier, the higher concentration of Mn^{4+} and chemically adsorbed oxygen on the surface of the catalyst, the higher reducibility, as well as the higher adsorption capacity for NH$_3$ and NO, thus exhibiting superior catalyst activity and sulfur resistance. Inorganic non-metallic minerals include cordierite,[92] montmorillonite,[93] diatomite,[94] and augite. Cordierite, as a bulk silicate mineral with a honeycomb shape and regular channel structure, is usually used as a monolithic carrier to achieve better catalyst performance.[95] It is one of the most widely used carriers for industrial catalysts.[96] Zhao et al.[97] first prepared monolithic catalysts of cordierite-supported Sm-modified Mn–Ce composite oxides by impregnation method and found that at Sm/Mn molar ratio of 0.1, Sm-MnCe/cordierite catalysts had a wide activity temperature window and the NO$_X$ removal rate was above 80% in the range of 60–270 °C ([NO] = [NH$_3$] = 500 ppm, [O$_2$] = 5 vol%, N$_2$ as the balanced gas and GHSV = 20 000 h^{-1}), while maintaining a high NO$_X$ conversion within 15 h at 100 ppm SO$_2$. The appropriate Sm content increases the specific surface area and acid sites, improves the redox environment, and enhances the Mn^{4+} content on the catalyst surface, which is conducive to the improvement of the catalytic activity. Attapulgite is a magnesium-aluminosilicate clay mineral with a layered chain structure, which has become a catalytic carrier for many catalytic reactions due to its unique natural one-dimensional structure, abundant surface functional groups, thermal stability and good moulding properties.[98] Li et al.[99] prepared Mn–Ce–Fe/attapulgite (ATP) monolithic catalysts by direct ink writing 3D printing technology to study the effect of different active

components on powdered catalysts in the SCR reaction. The effect of different active components in the SCR reaction on the powder catalyst was investigated. The results showed that the Mn–Ce–Fe/ATP powder catalysts contained higher Mn^{4+} and adsorbed state oxygen and more reducible substances at low temperatures, and the Mn–Ce–Fe/ATP powder catalysts exhibited excellent catalytic activity (90% NO conversion and 70% N_2 selectivity) in a wide temperature window range of 100–400 °C ([NO] = 1250 ppm, [NH_3] = 1268 ppm, [O_2] = 5 vol%, N_2 as the balanced gas and GHSV = 15 300 h^{-1}). Zhang et al.[100] used clay minerals (PG) as the substrate supported with Sb-modified MnO_X and found that Sb doping enhanced the dispersion of Mn on the carrier surface. In the presence of SO_2, Sb preferentially reacted with SO_2, protecting MnO_X as the active species from SO_2 sulfidation. Gu et al.[101] synthesized MnO_X–FeO_X catalysts with siliceous rock and titanium siliceous rock as supports by the wet impregnation method. They found that the latter exhibited excellent catalytic performance and H_2O resistance, which was attributed to the Ti in the titanium siliceous rock carrier, resulting in more acidic sites on the surface and stronger redox capacity of the active components.

3.5 Current status of various carriers

Metal oxide carriers are excellent substrates for manganese-based catalysts because of their high specific surface area, rich distribution of acidic sites and good catalytic thermal stability. However, a single metal oxide carrier is prone to cause accumulation of the active components when the catalyst is sintered. To address this, the carriers can be composited with the help of the advantages of different carriers and composite carriers can be prepared to enhance the catalytic activity of the carrier catalysts. Molecular sieve catalyst carriers have become good catalyst carriers with their unique pore structure, large specific surface area, good adsorption and high hydrothermal stability. However, the current research on molecular sieve carriers is mainly concentrated in the medium and high-temperature zone, lacking research on the SCR low-temperature zone, and sulfur poisoning and water poisoning are also key issues hindering the development of molecular sieve-based catalysts, thereby limiting their practical application. Carbon material carriers are often used as catalyst carriers because of their strong adsorption capacity, large specific surface area, rich pore structure, and numerous oxygen-containing groups. However, the single carbon-based catalysts have the disadvantages of poor stability in long-cycle operation, easy to oxidize at low temperatures, and poor resistance to SO_2 poisoning. These limitations often require surface modification to meet the demand for catalytic activity. At present, single catalyst carriers have certain defects in the catalytic process, and struggle to maintain efficient denitrification performance under the conditions of SO_2 and H_2O presence for a long period. Therefore, the development of efficient and stable green low-temperature denitrification catalysts is of great research significance. The composite carriers can take advantage of different carriers to carry out the composite carrier, realize the synergistic effect of "1 + 1 > 2", and improve the catalytic activity of the catalyst. Inorganic non-metallic mineral carriers should be further tapped for stable,

green, easily available, cheap and composite substances based on meeting the performance requirements.[102]

4 Mechanism of SCR denitrification reaction over Mn-based catalysts

So far, the NH_3-SCR reaction mechanism is still controversial, as different catalyst systems having different redox and acidic capacities, producing various NH_XNO_y active intermediates. These intermediates, in turn, affect the reaction path and reaction efficiency. The redox property determines the low-temperature activity of the catalyst, while the surface acidity determines the high-temperature activity of the catalyst, and thus, these two components are essential for a wide activity temperature window.[103,104] As shown in Fig. 9.

Depending on the reaction path of NO on the catalyst surface, the SCR catalytic reaction mechanism can be divided into the Langmuir–Hinshelwood (L–H) mechanism and the Eley–Rideal (E–R) mechanism.[26] The L–H mechanism assumes that NH_3(g) and NO_X(g) (NO and NO_2) are first adsorbed on the surface of the catalyst. The adsorbed NH_3 then interacts with the adsorbed active sites to produce either ammonia in the coordination state (NH_3-L, mainly from Lewis acid sites) or ionic ammonium (NH^{4+}, mainly from BrØnsted acid sites). These species subsequently react with nitrates and nitrites formed from adsorbed NO to produce the transition intermediate state product NH_XNO_y, which is then decomposed to N_2 and H_2O. The E–R mechanism suggests that the adsorbed NH_3 (NH_3-L and NH^{4+}) reacts with gaseous NO_X to produce the transition intermediate state product NH_XNO_y, which then decomposes to N_2 and H_2O. NH_3 can be adsorbed onto Lewis acid sites and BrØnsted acid sites, whereas NO is mainly physically adsorbed. The adsorption of NH_3 is considered to be the first step in the catalytic reaction process because NH_3 adsorbs more readily on acid sites than other reactive molecules.[105,106] Generally, the activation energy required for the reacting molecules of the L–H mechanism is lower, so that the L–H mechanism is more likely to occur than the E–R mechanism at low temperatures.

According to Kapteijn, Li and Fei et al.[15,107,108] on the NH_3-SCR reaction mechanism, the L–H mechanism reaction pathway is approximated as, where * and (g) represent the adsorption site and gas phase:
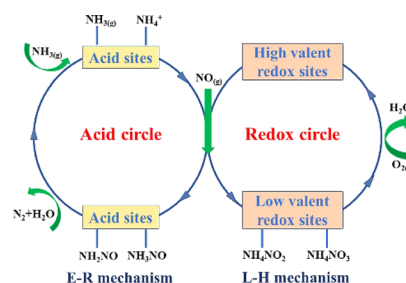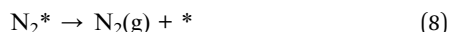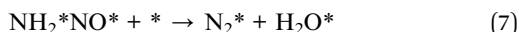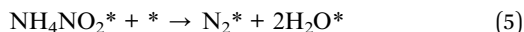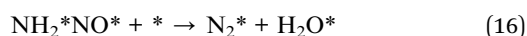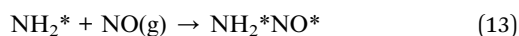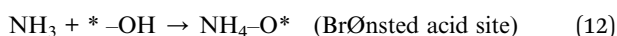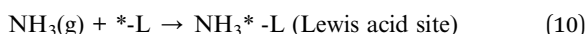

Fig. 9 Schematic diagram of NH_3-SCR reaction pathway on metal oxide and zeolite catalysts (reproduced from ref. 29 with permission from ACS Publications).

© 2024 The Author(s). Published by the Royal Society of Chemistry

$$NO + * \rightarrow NO* \tag{1}$$

$$NH_3 + * \rightarrow NH_2* + H* \tag{2}$$

$$NH_3 + * \text{–OH} \rightarrow NH_4\text{–O}* \tag{3}$$

$$NH_4* + NO* \rightarrow NH_4NO_2* \tag{4}$$

$$NH_4NO_2* + * \rightarrow N_2* + 2H_2O* \tag{5}$$

$$NH_2* + NO* \rightarrow NH_2*NO* \tag{6}$$

$$NH_2*NO* + * \rightarrow N_2* + H_2O* \tag{7}$$

$$N_2* \rightarrow N_2(g) + * \tag{8}$$

$$H_2O* \rightarrow H_2O(g) + * \tag{9}$$
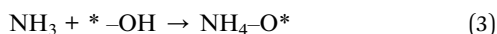
Li et al.[107] used first-principles calculations and believed that the E–R mechanism reaction pathway is:

$$NH_3(g) + *\text{-L} \rightarrow NH_3* \text{-L (Lewis acid site)} \tag{10}$$

$$NH_3* + * \rightarrow NH_2* + H* \tag{11}$$

$$NH_3 + * \text{–OH} \rightarrow NH_4\text{–O}* \quad \text{(BrØnsted acid site)} \tag{12}$$

$$NH_2* + NO(g) \rightarrow NH_2*NO* \tag{13}$$

$$NH_4* + NO(g) \rightarrow NH_4NO_2* \tag{14}$$

$$NH_4NO_2* + * \rightarrow NH_2*NO* + H_2O* \tag{15}$$

$$NH_2*NO* + * \rightarrow N_2* + H_2O* \tag{16}$$

$$N_2* \rightarrow N_2(g) + * \tag{17}$$

$$H_2O* \rightarrow H_2O(g) + * \tag{18}$$

Kapteijn et al.[15] believed that the denitrification pathway on pure MnO_X follows the E–R mechanism, and the interaction between NO, NH_3 and O_2 on manganese oxides is explained by the model involves NH_3 being continuously dehydrogenated by surface oxygen. As shown in Fig. 10.

Ramis et al.[109] conducted FT-IR research on the NH_3-SCR reaction and proposed a more complete E–R reaction pathway based on the above model, as shown in Fig. 11 below.

Qi et al.[110] found that gaseous NH_3 molecules are first adsorbed on MnO_X–CeO_2 catalysts to form coordinated NH_3, which is then oxidized to produce NH_2 and OH, and NO molecules are also adsorbed on MnO_X–CeO_2 catalysts, which are then oxidized to nitrates and nitrites. The reaction of NH_2 and NO produces nitrosamines (NH_2NO), which then decompose NH_2NO to N_2 and H_2O. Nitrous acid is produced by the reaction in oxidation or denitrification of $2NO_2$ and H_2O. Nitrite reacts with ammonia to produce ammonium nitrate, which is equivalent to nitrosamine hydrate (NH_2NO), and both ammonium nitrite and nitrosamine are unstable intermediates, which are intermediates in numerous NH_3-SCR reaction mechanisms. The reaction mechanism of NO and NH_3 on the surface of the
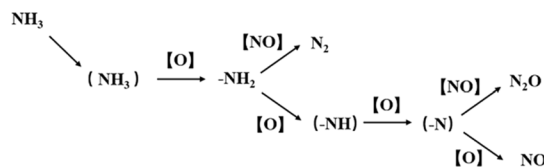

Fig. 10 NH_3 activation model on MnO_X (reproduced from ref. 15 with permission from ACS Publications.).
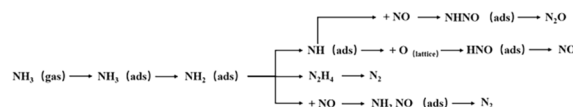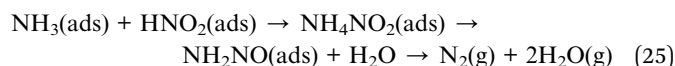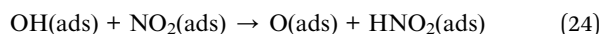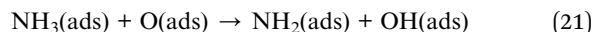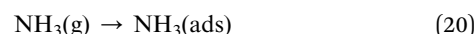

Fig. 11 Mechanism diagram of NH_3 stepwise oxidation activation and NO reaction during NH_3-SCR process (reproduced from ref. 109 with permission from ACS Publications.).

MnO_X–CeO_2 catalyst is as follows, where ads represents the adsorbed state:

$$O_2(g) \rightarrow 2O(ads) \tag{19}$$

$$NH_3(g) \rightarrow NH_3(ads) \tag{20}$$

$$NH_3(ads) + O(ads) \rightarrow NH_2(ads) + OH(ads) \tag{21}$$

$$NO(g) + 1/2O_2(g) \rightarrow NO_2(ads) \tag{22}$$

$$NH_2(ads) + NO(g) \rightarrow NH_2NO(ads) \rightarrow N_2(g) + H_2O(g) \tag{23}$$

$$OH(ads) + NO_2(ads) \rightarrow O(ads) + HNO_2(ads) \tag{24}$$

$$NH_3(ads) + HNO_2(ads) \rightarrow NH_4NO_2(ads) \rightarrow$$
$$NH_2NO(ads) + H_2O \rightarrow N_2(g) + 2H_2O(g) \tag{25}$$

The NH_3-SCR reaction process does not follow a single reaction mechanism, and many studies have shown that most of the reaction mechanisms of the current low-temperature NH_3-SCR catalysts are the simultaneous existence of the L–H mechanism and the E–R mechanism, and even different temperature segments have different reaction mechanisms. For instance, at temperatures below 150 °C, the increased NO oxidation predominantly facilitates the Langmuir–Hinshelwood (L–H) mechanism on the catalyst surface. Conversely, at temperatures above 150 °C, the augmented NH_3 adsorption capacity primarily promotes the Eley–Rideal (E–R) mechanism.[111] Different species dominate the adsorption at acid sites on the catalyst surface depending on the temperature. Specifically, at lower temperatures, coordinated NH_3 adsorbed on Lewis acid sites is predominant. As the temperature increases, NH^{4+} adsorbed on BrØnsted acid sites becomes the leading species.[112]

Gu et al.[113] simulated the gas adsorption process on the Mn active centres on the MnO_X/SiO_2 β-cristobalite (101) surface based on density functional theory. Under anaerobic conditions, NO was more readily adsorbed on the surface of Mn_2O_3/SiO_2 β-cristobalite (101), while NH_3 was more readily adsorbed

on the surface of MnO_2/SiO_2 β-cristobalite (101). The NO adsorption reaction mainly followed the L–H mechanism, whereas the NH_3 adsorption reaction mainly followed the E–R mechanism, and the O_2 adsorption processes on the Mn active centres of the two catalysts were similar. The main reason for the better catalytic activity of MnO_2/SiO_2 than that of Mn_2O_3/SiO_2 is the difference in NH_3 adsorption energy between the catalysts.

Wang et al.[114] investigated the reaction mechanism of the synergistic effect of MnO_X–CeO_2 in the NH_3-SCR reaction based on experimental and density-functional theory and found that the synergistic effect is to promote the catalytic activity through the formation of surface oxygen induced by the electron transfer between Ce^{4+} and Mn^{2+}, and the establishment of Mn redox cycle and Ce redox cycle to activate the NH_3 and O_2, respectively. Firstly, owing to the oxidizing ability of Ce^{4+} in E-CeO_2, a reaction takes place between Ce^{4+} and Mn^{2+}: $Ce^{4+} + Mn^{2+} \rightarrow Mn^{3+} + Ce^{3+}$. Concurrently, surface oxygen vacancies (O_V) are generated and stabilised on the surface of E-CeO_2. These surface oxygen vacancies significantly enhance the adsorption and dissociation of O_2, thereby oxidising Ce^{3+} back to Ce^{4+}. The resultant dissociated O atoms further oxidise Ce^{3+} and occupy the surface oxygen vacancies, thus forming a Ce redox cycle. Gaseous NO is adsorbed onto the E-CeO_2 lattice oxygen near the MnO_X clusters, manifesting as nitrites and nitrates. Simultaneously, NH_3 coordinates with Mn^{3+} species (Lewis acid sites) and is subsequently activated by the nearby Mn_{3+} ions. The activated NH_3 then reacts with NO to yield N_2 and H_2O, during which a Mn^{3+} ion is reduced to Mn^{2+}. After H* atoms diffuse from Mn–OH to form Ce–OH, the Mn^{2+} ions are oxidised back to Mn^{3+} by Ce^{4+}, completing the Mn redox cycle. Fig. 12 illustrates the schematic diagram of the synergistic effect mechanism of the Mn/E-CeO_2 catalyst.

Li et al.[115] investigated the mechanism of NO reduction and N_2O formation, and suggested a possible mechanism on Fe–Mn/SBA-15 catalysts. The Fe–Mn/SBA-15 catalyst primarily follows the L–H mechanism at low temperatures (200 °C). However, as the temperature increases, the E–R mechanism becomes more prominent and dominates at higher temperatures (250 °C). Since Fe–Mn/SBA-15 is a strongly alkaline catalyst, the adsorption capacity of NH_3 on the molecular sieve is
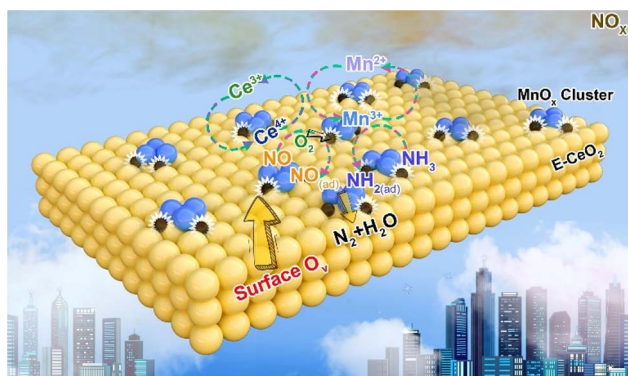

Fig. 12 Schematic reaction mechanism of MnO_X–CeO_2 catalyst synergistic effect (reprinted from ref. 114. Copyright 2023, with permission from Elsevier).

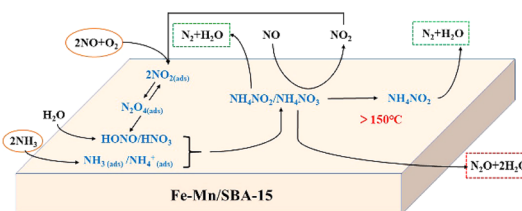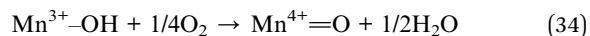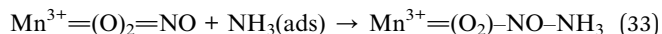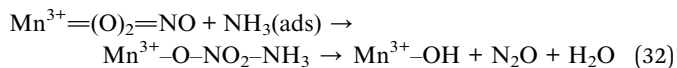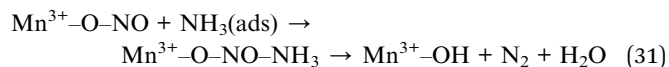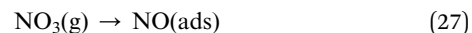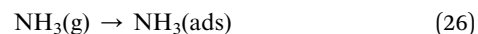Fig. 13 Low temperature NH_3-SCR reaction mechanism of Fe Mn/SBA-15 catalyst (reproduced from ref. 115 with permission from ACS Publications.).
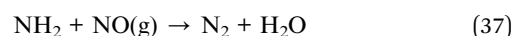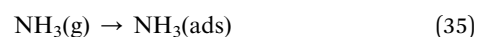
weak, while the adsorption of NO and O_2 onto the molecular sieve surface is strong. The adsorbed species form intermediates, NH_4NO_2 or NH_4NO_3, where NH_4NO_2 decomposes into N_2O and H_2O. This process aligns with the L–H mechanism. The generated intermediate NH_4NO_3 can react with gaseous NO to produce NH_4NO_2 and NO_2. Furthermore, NH_4NO_3 can directly decompose to produce NO and H_2O. The entire process adheres to the E–R mechanism. The denitrification process of the Fe–Mn/SBA-15 catalyst during the SCR reaction is illustrated in Fig. 13.

Yang et al.[116] investigated the mechanism of N_2O and NO generation in the low-temperature NH_3-SCR process of Mn–Fe spinel using in situ diffuse reflectance Fourier transform infrared spectroscopy (in situ DRIFTS) and transient reactions, and found that the L–H mechanism and the E–R mechanism existed simultaneously in the SCR reaction. As shown in Fig. 14.

The L–H mechanism on Mn–Fe spinel catalysts was developed as follows:[105,117]

$$NH_3(g) \rightarrow NH_3(ads) \tag{26}$$

$$NO_3(g) \rightarrow NO(ads) \tag{27}$$

$$Mn^{4+}{=}O + NO(ads) \rightarrow Mn^{3+}{-}O{-}NO \tag{28}$$

$$Mn^{3+}{-}O{-}NO + 1/2O_2 \rightarrow Mn^{3+}{-}O{-}NO_2 \tag{29}$$

$$Mn^{3+}{-}O{-}NO + 1/2O_2 \rightarrow Mn^{3+}{=}(O)_2{=}NO \tag{30}$$

$$\begin{aligned}Mn^{3+}{-}O{-}NO + NH_3(ads) \rightarrow \\ Mn^{3+}{-}O{-}NO{-}NH_3 \rightarrow Mn^{3+}{-}OH + N_2 + H_2O\end{aligned} \tag{31}$$

$$\begin{aligned}Mn^{3+}{=}(O)_2{=}NO + NH_3(ads) \rightarrow \\ Mn^{3+}{-}O{-}NO_2{-}NH_3 \rightarrow Mn^{3+}{-}OH + N_2O + H_2O\end{aligned} \tag{32}$$

$$Mn^{3+}{=}(O)_2{=}NO + NH_3(ads) \rightarrow Mn^{3+}{=}(O_2){-}NO{-}NH_3 \tag{33}$$

$$Mn^{3+}{-}OH + 1/4O_2 \rightarrow Mn^{4+}{=}O + 1/2H_2O \tag{34}$$

The Eley–Rideal principle on Mn–Fe spinel catalysts was as follows:[105,117]

$$NH_3(g) \rightarrow NH_3(ads) \tag{35}$$

$$NH_3(ads) + Mn^{4+}{=}O \rightarrow NH_2 + Mn^{3+}{-}OH \tag{36}$$

$$NH_2 + NO(g) \rightarrow N_2 + H_2O \tag{37}$$
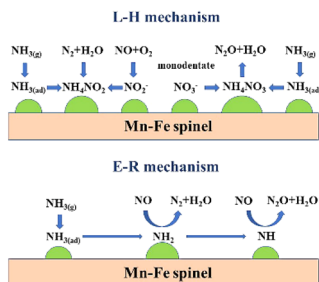
Fig. 14 Schematic diagram of the coexistence of L–H and E–R mechanisms on Mn–Fe spinel catalyst (reproduced from ref. 116 with permission from ACS Publications).

$$NH_2 + Mn^{4+}=O \rightarrow NH + Mn^{3+}-OH \quad (38)$$

$$NH + NO(g) + Mn^{4+}=O \rightarrow N_2O + Mn^{3+}-OH \quad (39)$$

$$Mn^{3+}-OH + 1/4O_2 \rightarrow Mn^{4+}=O + 1/2H_2O \quad (40)$$
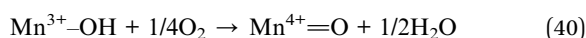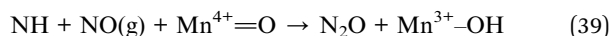
Zhang et al.[118] prepared manganese-based SCR catalysts using homemade pyrolysis coke as the carrier, analyzing the catalytic mechanism of Mn@$_X$/C (@ is Ce, Mo or Co) catalysts and found that the mechanism of SCR reaction was:

$$NH_3(g) + Mn-OH \rightarrow NH^{4+}(ads)-O-Mn \quad (BrØnsted\ acid\ site) \quad (41)$$
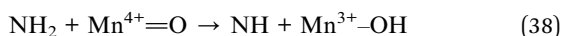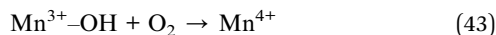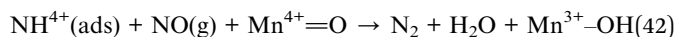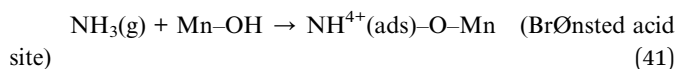
$$NH^{4+}(ads) + NO(g) + Mn^{4+}=O \rightarrow N_2 + H_2O + Mn^{3+}-OH (42)$$

$$Mn^{3+}-OH + O_2 \rightarrow Mn^{4+} \quad (43)$$

Yu et al.[119] conducted a reaction mechanism study of loaded MnO$_X$/MWCNTS using the in situ DRIFTS technique and discussed the intermediates and NH$_3$-SCR reaction pathways during denitrification of MnO$_X$/MWCNTS catalysts at 210 °C, and proposed two possible reaction pathways. One is the reaction of the NO$_X$ active component with NH^{4+} to produce NH$_4$N$_2$O$_4$(a), NH$_4$NO$_2$(a) or NH$_4$NO$_3$(a) intermediates and ultimately generates N$_2$ and H$_2$O. The other pathway is that NH$_3$ is first adsorbed on the active site to generate NH$_2$, and then NH$_2$ reacts with the NO$_x$ active component to generate the unstable intermediates NH$_2$NO$_2$ or NH$_2$NO$_3$, which then decompose into N$_2$ and H$_2$O. This is illustrated in Fig. 15.

Although the mechanism of NH$_3$-SCR reaction has been studied extensively, due to the complexity of the actual working flue gas conditions and the different mechanisms of Mn-based catalysts, it is necessary to further investigate the reaction mechanisms contained in NH$_3$-SCR catalysts in-depth and to combine kinetics, solid surface chemistry, and computational chemistry to give the mechanism of NH$_3$-SCR reaction of Mn-based catalysts.

5 Poisoning mechanism of Mn-based catalysts in NH$_3$-SCR

The flue gas composition is complex. Even after purification by dust removal and desulfurization equipment, there will be
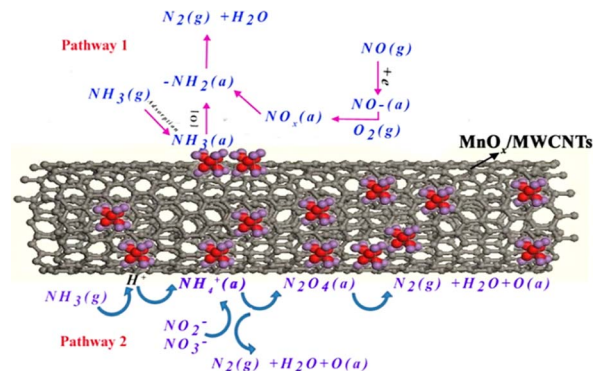

Fig. 15 Schematic diagram of two reaction pathways on MnO$_X$/MWCNTS catalyst at 210 °C (reprinted from ref. 119. Copyright 2015, with permission from AAGR Aerosol and Air Quality Research.).

a small amount of H$_2$O and SO$_2$ in the processed flue gas.[120] The manganese catalyst is more sensitive to the residual deactivation substances in the flue gas. Once poisoned and deactivated, its denitrification performance will be severely impacted. Therefore, it is required that the catalyst has a high sulfur resistance and water resistance,[121] so the study of the manganese catalyst poisoning mechanism is crucial for the realization of the practical application of the catalyst.

5.1 Mechanism of H$_2$O poisoning

Water vapour will greatly reduce the catalytic activity of the catalyst in the low-temperature SCR reaction. The deactivation of catalysts by water vapour is divided into reversible and irreversible deactivation.[64,122] The reversible deactivation of the catalyst by H$_2$O vapor is usually considered to be the competitive adsorption of H$_2$O with NO and NH$_3$ on the catalyst surface, which occupies the active sites and leads to lower reactant adsorption reducing the NO$_X$ conversion rate. However, the inhibition will disappear gradually with the increase in temperature. Liu et al.[123] by comparing the deNO$_X$ performance of β-MnO$_2$ and Co–MnO$_2$ catalysts in the presence of water vapour, found that water vapour will form competitive adsorption with NH$_3$ and inhibit the adsorption and interfacial reaction of NH$_3$ on the surface of the catalysts. This lower NH$_3$ adsorption leads to poorer NO$_X$ conversion rate. However, H$_2$O molecules have a reversible effect on the gas adsorption on the catalyst surface and thus have a slight impact on the NH$_3$-SCR activity,[124] which is the same as Xiong et al.[125] found that the presence of water affects the effect of the SCR performance of Mn–Fe spinel. In the absence of water vapour, the NO$_X$ conversion rate of Mn–Fe spinel exceeds 80% at temperatures above 140 °C. However, the addition of 5% water vapour significantly reduces the NO$_X$ conversion rate, reaching only 40% at 140 °C ([NO] = [NH$_3$] = 500 ppm, [O$_2$] = 2 vol%, N$_2$ as the balanced gas and GHSV = 120 000 h^{-1}). The presence of water forms competitive adsorption with the reacting molecules, which reduces the oxidation capacity of the catalyst and inhibits the occurrence of its interfacial reaction, resulting in a decrease in the catalytic activity. Yan et al.[126] also discovered that high

humidity conditions not only reduce acidity and hinder the adsorption of NH_3 on the catalyst surface, but also that the dissolution of water molecules affects the structure of the catalyst, leading to a decrease in the dispersion of the active components. With the introduction of 35% water vapour, the activity of the Co–Mn–Ce/TiO_2 (stearic acid) catalyst stabilises at approximately 30%. ([NO] = [NH_3] = 600 ppm, [O_2] = 5 vol%, N_2 as the balanced gas and GHSV = 15 000 h^{-1}). But the activity of the catalyst is restored when the introduction of H_2O is ceased. Similarly, Lin et al.[127] and Hu et al.[128] found that the adverse effect of H_2O on the catalyst was reversible when the introduction of H_2O was stopped. The irreversible deactivation of the catalyst by H_2O vapour is typically attributed to the decomposition of H_2O into hydroxyl radicals on the catalyst surface, leading to the blocking of the active sites, and resulting in a decrease in the denitrification activity and is irreversible.[129] Moreover, hydroxyl radicals can only be dissociated at high temperatures (252–502 °C). After Liu et al.[130] introduced water vapour into the $Fe_{0.75}Mn_{0.25}TiO_X$ catalyst, the hydroxyl groups produced by the decomposition of water molecules caused a transformation of some Lewis acid sites into BrØnsted acid sites. This resulted in a decrease in the intensities of the corresponding wavelengths of NH_3 and NO_X, leading to a reduction in the catalyst's denitrification activity. Similarly, Yan et al.[126] also observed that under humid conditions, water molecules adsorbed onto the surface of the Co–Mn–Ce/TiO_2 catalyst to form hydroxyl groups. These hydroxyl groups had an irreversible impact on the SCR denitrification process.[131]

5.2 Mechanism of SO_2 poisoning

While some studies suggest that catalyst SO_2 poisoning is reversible,[132,133] the majority of research indicates that its effects are irreversible.[134,135] The impact of SO_2 on the catalyst accumulates over time, ultimately resulting in a sustained and irreversible decline in catalytic activity. The deactivation mechanism of catalyst SO_2 poisoning can be categorised into three cases:[136–138] Firstly, SO_2 in the flue gas is oxidised to SO_3 by the catalyst. This SO_3 subsequently reacts with NH_3 to form $(NH_4)_2SO_4$ and NH_4HSO_4, which deposit onto the catalyst surface, blocking active sites and obstructing the pore structure. This process leads to a reduction in catalytic activity. Secondly, SO_2 competes with the reactants for adsorption sites, hindering the catalytic reaction process. When both SO_2 and NO are present in the flue gas, they compete for adsorption sites. SO_2 preferentially occupies these sites, leading to the sulfation of the catalyst. Thirdly, SO_2 can react directly with the active components of the catalyst, resulting in the sulfation of the active metal atoms. This process deactivates the catalyst and disrupts the redox cycle of the active phase. Zhang et al.[139] discovered that SO_2 readily oxidised to SO_3 on the surface of MnO_X/palygorskite (PG) catalysts, leading to the formation of polysulfuric acid. This acid encapsulated the active components and blocked the micropores, causing the initial deactivation of the MnO_X/PG catalysts. The subsequent deposition of ammonium sulfate was not the primary cause of deactivation. As illustrated in Fig. 16. Xiao et al.[140] proposed that the inhibition

of NO conversion by SO_2 was due to competitive adsorption on the active sites of the catalyst. The adsorbed SO_2 was then further oxidised to inactive sulfate on the catalyst surface. Jiang et al.[141] suggested that the addition of SO_2 reduced the oxidation performance and surface acidity of the catalyst inhibiting NO_x conversion. Xiong et al.[142] found that the irreversible deactivation of the Mn_3O_4 spinel catalysts was primarily cause by the reaction of SO_2 with Mn atoms in the active centre, resulting in the formation of $MnSO_4$. This finding aligns with Chen et al.,[143] who concluded that MnO_X catalysts are poisoned by SO_2, leading to the formation of $MnSO_4$ on the surface, rather than $(NH_4)_2SO_4$ and NH_4HSO_4. This sulfation of the active Mn atoms reduces the number of active components and reactive sites, ultimately decreasing catalytic activity.

In practice, SO_2 and H_2O coexist in the flue gas, and their poisoning effect on the catalyst exhibits a synergistic effect. This exacerbates the formation of sulfate and accelerates catalyst deactivation. Consequently, it is essential that the catalysts under investigation possess resistance to both sulfur and water. Common methods for enhancing catalyst performance and resistance to sulfur and water include metal modification or doping, selection of appropriate carriers, and the rational design of morphology and structure.[122] Generally, manganese-based catalysts have high low-temperature catalytic activity, but their tolerance to SO_2 and H_2O limits their industrial applications. Therefore, researchers modify or dope them by adding metal elements to improve their resistance to sulfur and water. CeO_2, with an excellent oxidative reduction ability, is often employed as a catalyst additive or carrier. Ce, acting as a sacrificial agent, preferentially reacts with SO_2 to form $CeSO_4$. This compound is easier to decompose than $MnSO_4$, thus preventing the formation of $MnSO_4$, which would otherwise deposit on the acidic sites of the catalyst surface and cause poisoning. By preferentially reacting with SO_2, Ce effectively avoids the poisoning of the catalyst and increases the number of acidic sites on its surface.[144] Yoon et al.[145] synthesised Ce-doped Mn–Cr layered structure catalysts using a co-precipitation method. Their research demonstrated that Ce doping effectively inhibits the formation of manganese sulphate on the catalyst surface, reduces the decomposition temperature of ammonium sulphate, and enhances both the acidity and reducibility of the catalyst surface. These improvements contribute to a significant enhancement in the SO_2 resistance of Mn catalysts. Both Sb and Ce, as rare earth metals, possess the ability to enhance sulfur and water resistance. Yan et al.[146]
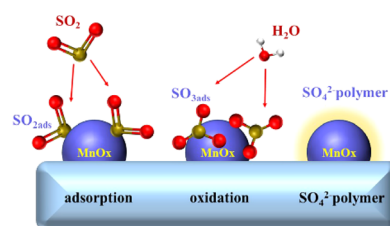

Fig. 16 SO_2 poisoning process on the surface of MnO_X/PG catalyst (reproduced from ref. 139 with permission from MDPI.).

prepared Sb-modified $Mn–Ce–Sb_X/TiO_2$ catalysts using the impregnation method. Their findings indicated that the addition of Sb effectively inhibits the formation of sulphate on the catalyst surface in the presence of SO_2 and H_2O.[147–149] Zhang et al.[100] also observed that doping Sb into the MnO_X/palygorskite (PG) catalyst significantly inhibited the sulphation of the active phase. Simultaneously, Sb promoted the dispersion of MnO_X on the carrier surface. The preferential reaction between SbO_X and SO_2 effectively protected the active MnO_X from sulfation by SO_2, thus enhancing the catalyst's tolerance to SO_2. A suitable hydrophobic carrier not only provides a large specific surface area and numerous pore structures to enhance catalyst acidity but also plays a crucial role in the synergistic effect between the carrier and the active component, significantly impacting the catalyst's resistance to sulfur water.[150] Pure Al_2O_3, with its large specific surface area and abundant acidic sites,[151,152] promotes good dispersion of the active substances. Additionally, it provides ample adsorption sites for reactants,[153] facilitating the adsorption of chemically adsorbed oxygen on the catalyst surface, thereby exhibiting improved sulfur and water resistance. Liu et al.[73] prepared Mn-based catalysts supported on γ-Al_2O_3, TiO_2, and MCM-41 using an impregnation method. They observed that pure γ-Al_2O_3 provided abundant adsorption sites and that a strong interaction existed between Mn and γ-Al_2O_3. The Mn/γ-Al_2O_3 catalyst exhibited the strongest NO adsorption performance and good SO_2 tolerance. Rational morphology and structural design are also effective measures for enhancing the sulfur and water resistance of catalysts. The unique pore structure of TiO_2 nanotubes, combined with their large specific surface area, numerous acidic sites, and reactive oxygen species on the surface, makes them ideal as catalyst carriers. These properties collectively contribute to enhancing the low-temperature denitrification activity of manganese-based catalysts and improving their resistance to sulfur and water resistance.[154,155] Qin et al.[156] synthesised a TiO_2 support using a hydrothermal method and subsequently prepared a novel flower-shaped $MnCe/TiO_2$ catalyst. Their research revealed that the active species of the $MnCe/TiO_2$-Flower catalyst exhibited high dispersion, abundant acid sites, a large specific surface area, and excellent redox properties. This catalyst achieved a NO conversion rate of approximately 100% at 150–250 °C, a N_2 selectivity exceeding 80% at 150–350 °C ($[NO] = [NH_3] = 600$ ppm, $[O_2] = 5$ vol%, Ar as the balanced gas and GHSV = 108 000 h^{-1}), and demonstrated excellent tolerance to SO_2 and H_2O ($[SO_2] = 100$ ppm, $[H_2O] = 5$ vol%). In summary, the poisoning of low-temperature manganese-based catalysts by H_2O and SO_2 is intricately linked to the catalytic reaction process. This includes competitive adsorption of H_2O and NH_3 on the catalyst surface, SO_2-induced acidification of active centre atoms, and the occupation of active sites by deposited $(NH_4)_2SO_4$ and NH_4HSO_4. These phenomena are directly related to the physicochemical properties of the manganese-based catalysts. Therefore, to enhance the H_2O/SO_2 resistance of these catalysts during the SCR process, a top-level design approach is required, considering the catalytic mechanism. This involves strategies such as employing hydrophobic materials, constructing a unique core–shell structure, modifying the catalyst through metal doping, and integrating DFT theoretical calculations. By screening for SO_2 and incorporating spatial barriers into the material design, the anti-H_2O/SO_2 performance of manganese-based catalysts can be significantly improved.[157]

6 Conclusions and outlook

Manganese-based catalysts have emerged as a research hotspot due to their excellent low-temperature denitrification performance. While single manganese-based catalysts exhibit promising NH_3-SCR catalytic activity, they suffer from a narrow operating temperature window and poor water and sulfur resistance. Multicomponent manganese-based catalysts, obtained through modification by incorporating transition metals or rare earth elements, demonstrate superior catalytic activity, high denitrification efficiency, and improved water and sulfur resistance. Supported manganese-based catalysts, owing to the presence of carriers, benefit from a large surface area, strong surface acidity, and a high density of active sites. These properties contribute to their excellent low-temperature NO_X removal efficiency, N_2 selectivity, a wider operating temperature window, and enhanced water and sulfur resistance. Research on Mn-based denitrification catalysts have yielded significant results, highlighting the practical importance of further investigating low-temperature Mn-based denitrification catalysts with high activity and stability. These catalysts hold promise for industrial application and commercialisation. Future research should focus on the following aspects:

(1) While significant progress has been made in enhancing catalyst resistance to SO_2/H_2O, the long-term durability and stability of these catalysts in the continuous presence of SO_2/H_2O require further in-depth exploration.

(2) MnO_X has been modified by introducing other metal oxides to enhance the catalytic activity of low-temperature NH_3-SCR. The prevailing explanation for this enhancement is that MnO_X possesses strong redox properties (high-valent Mn^{4+}), a high density of surface defects and acidic sites, a large surface area, and significant surface chemical adsorption of oxygen. However, the underlying mechanisms requires further in-depth study.

(3) Currently, the simulated gas composition used in SCR denitrification reaction studies is simplified, leading to overly idealised experimental results. Future research should focus on conducting industrial-scale tests to verify the denitrification performance, water and sulfur resistance, and reaction mechanisms under actual operating conditions.

(4) Currently, there is limited research on the impact of catalyst forming technology on catalyst performance. In-depth studies are needed to investigate the trends in catalytic activity under different moulding process conditions. For instance, coated honeycomb catalysts and extruded honeycomb catalysts have demonstrated promising advantages in terms of high catalytic activity. Further research is warranted in this area.

(5) While the L–H and E–R mechanism of the SCR denitrification reaction have been extensively studied in the literature, the NH_3-SCR reaction mechanism at low temperatures remains unclear. Techniques such as in situ DRIFTS, in situ Raman

spectroscopy, and computational molecular simulation could provide valuable insights into the adsorption states of NH_3, NO, O_2, SO_2, and H_2O on the catalyst surface. By monitoring the reaction process, we can elucidate the reaction mechanism of low-temperature NO_X removal and develop a comprehensive reaction mechanism that can explain the NH_3-SCR reaction mechanism.

(6) Optimising catalyst structure design, extending catalyst operating cycles based on real-world operating conditions, and carefully considering the balance between catalyst cost and performance are crucial steps in developing more efficient, stable, and environmentally friendly low-temperature SCR denitrification catalysts for industrial applications.

Data availability

No primary research results, software or code have been included and no new data were generated or analysed as part of this review.

Author contributions

Jiadong Zhang: conception, investigation, writing-review and editing; Zengyi Ma: methodology, review and editing; Ang Cao: methodology, review and editing; Jianhua Yan: methodology, review and editing; Yuelan Wang: investigation and methodology; Miao Yu: investigation and methodology; Linlin Hu: investigation and methodology; Shaojing Pan: investigation and methodology. All authors have read and agreed to the published version of the manuscript.

Conflicts of interest

There are no conflicts to declare.

Acknowledgements

References

1 Y. Shi, Y. Xia, B. Lu, N. Liu, L. Zhang, S. Li and W. Li, *J. Zhejiang Univ., Sci., A*, 2014, **15**, 454–464.

2 L. Chen, Q. Wang, X. Wang, Q. Cong, H. Ma, T. Guo, S. Li and W. Li, *Chem. Eng. J.*, 2020, **390**, 124251.

3 Y. Shan, J. Du, Y. Yu, W. Shan, X. Shi and H. He, *Appl. Catal., B*, 2020, **266**, 118655.

4 X. X. Cheng and X. T. T. Bi, *Particuology*, 2014, **16**, 1–18.

5 M. Fu, C. Li, P. Lu, L. Qu, M. Zhang, Y. Zhou, M. Yu and Y. Fang, *Catal. Sci. Technol.*, 2014, **4**, 14–25.

6 R. Zhang, N. Liu, Z. Lei and B. Chen, *Chem. Rev.*, 2016, **116**, 3658–3721.

7 G. Busca, L. Lietti, G. Ramis and F. Berti, *Appl. Catal., B*, 1998, **18**, 1–36.

8 Z. Xiong, C. Wu, Q. Hu, Y. Wang, J. Jin, C. Lu and D. Guo, *Chem. Eng. J.*, 2016, **286**, 459–466.

9 Z. Huang, X. Gu, W. Wen, P. Hu, M. Makkee, H. Lin, F. Kapteijn and X. Tang, *Angew. Chem., Int. Ed.*, 2013, **52**, 660–664.

10 D. Damma, P. R. Ettireddy, B. M. Reddy and P. G. Smirniotis, *Catalysts*, 2019, **9**, 349.

11 Z. Liu, B. Jia, Y. Zhang and M. Haneda, *Ind. Eng. Chem. Res.*, 2020, **59**, 13916–13922.

12 S. Pan, H. Luo, L. Li, Z. Wei and B. Huang, *J. Mol. Catal. A: Chem.*, 2013, **377**, 154–161.

13 Y. Ma, F. Gao, G. Jia, S. Huang, S. Zhao, H. Yi and X. Tang, *Mod. Chem. Ind.*, 2019, **39**, 33–37.

14 Y. Zheng and X. Wang, *Funct. Mater.*, 2014, **45**, 11008–11012.

15 F. Kapteijn, L. Singoredjo, A. Andreini and J. A. Moulijn, *Appl. Catal., B*, 1994, **3**, 173–189.

16 X. Tang, J. Hao, W. Xu and J. Li, *Catal. Commun.*, 2007, **8**, 329–334.

17 J. Zhou, B. Wang, J. Ma, G. Li, Q. Sun, W. Xu and Y. Li, *Environ. Chem.*, 2018, **37**, 782–791.

18 G. He, M. Gao, Y. Peng, Y. Yu, W. Shan and H. He, *Environ. Sci. Technol.*, 2021, **55**, 6995–7003.

19 L. Ye, P. Lu, X. Chen, P. Fang, Y. Peng, J. Li and H. Huang, *Appl. Catal., B*, 2020, **277**, 119257.

20 H. Liu, X. Li, Q. Dai, H. Zhao, G. Chai, Y. Guo, Y. Guo, L. Wang and W. Zhan, *Appl. Catal., B*, 2021, **282**, 119577.

21 Z. Zhang, J. Li, J. Tian, Y. H. Zhong, Z. Zou, R. Dong, S. Gao, W. B. Xu and D. L. Tan, *Fuel Process. Technol.*, 2022, **230**, 107213.

22 J. Huang, H. Huang, L. Liu and H. Jiang, *Mol. Catal.*, 2018, **446**, 49–57.

23 F. Kapteijn, J. RodriguezMirasol and J. A. Moulijn, *Appl. Catal., B*, 1996, **9**, 25–64.

24 W. Shan and H. Song, *Catal. Sci. Technol.*, 2015, **5**, 4280–4288.

25 J. Yang, PhD thesis, Chongqing University,China, 2022, , DOI: 10.27670/d.cnki.gcqdu.2022.000390.

26 C. Liu, J. Shi, C. Gao and C. Niu, *Appl. Catal., A*, 2016, **522**, 54–69.

27 X. Tang, J. Li, L. Sun and J. Hao, *Appl. Catal., B*, 2010, **99**, 156–162.

28 C. L. Yu, B. C. Huang, L. F. Dong, F. Chen and X. Q. Liu, *Catal. Today*, 2017, **281**, 610–620.

29 L. Han, S. Cai, M. Gao, J. Hasegawa, P. Wang, J. Zhang, L. Shi and D. Zhang, *Chem. Rev.*, 2019, **119**, 10916–10976.

30 J. Liu, Y. Wei, P. Li, P. Zhang, W. Su, Y. Sun, R. Zou and Y. Zhao, *ACS Catal.*, 2018, **8**, 3865–3874.

31 S. Andreoli, F. A. Deorsola, C. Galletti and R. Pirone, *Chem. Eng. J.*, 2015, **278**, 174–182.

32 P. Gong, J. Xie, D. Fang, D. Han, F. He, F. Li and K. Qi, *Chin. J. Catal.*, 2017, **38**, 1925–1934.

33 B. Zhao, R. Ran, X. Wu and D. Weng, *Appl. Catal., A*, 2016, **514**, 24–34.

34 Q. Yu, J. Xiong, Z. Li, X. Mei, P. Zhang, Y. Zhang, Y. Wei, Z. Zhao and J. Liu, *Catal. Today*, 2021, **376**, 229–238.

35 W. Tian, H. Yang, X. Fan and X. Zhang, *J. Hazard. Mater.*, 2011, **188**, 105–109.

36 J. Shi, C. Gao, C. Liu, Z. Fan, G. Gao and C. Niu, *J. Nanopart. Res.*, 2017, **19**, 194.

37 N. Husnain, E. Wang, K. Li, M. T. Anwar, A. Mehmood, M. Gul, D. Li and J. Mao, *Rev. Chem. Eng.*, 2019, **35**, 239–264.

38 X. Leng, Z. Zhang, Y. Li, T. Zhang, S. Ma, F. Yuan, X. Niu and Y. Zhu, *Fuel Process. Technol.*, 2018, **181**, 33–43.

39 Q. Huang, H. Si, S. Yu, J. Wang, T. Tao, B. Yang, Y. Zhao and M. Chen, *Environ. Technol.*, 2020, **41**, 1664–1676.

40 X. Tang, C. Wang, F. Gao, Y. Ma, H. Yi, S. Zhao and Y. Zhou, *J. Environ. Chem. Eng.*, 2020, **8**, 104399.

41 S. Xiong, Y. Peng, D. Wang, N. Huang, Q. Zhang, S. Yang, J. Chen and J. Li, *Chem. Eng. J.*, 2020, **387**, 124090.

42 X. Wang, R. Duan, W. Liu, D. Wang, B. Wang, Y. Xu, C. Niu and J. Shi, *Appl. Surf. Sci.*, 2020, **510**, 145517.

43 K. Zhu, W. Yan, S. Liu, X. Wu, S. Cui and X. Shen, *Appl. Surf. Sci.*, 2020, **508**, 145024.

44 J. Rong, W. Zhao, W. Luo, K. Kang, L. Long, Y. Chen and X. Yao, *J. Rare Earths*, 2023, **41**, 1323–1335.

45 M. T. Le, S. Singh, M. Nguyen-Quang, A. B. Ngo, A. Bruckner and U. Armbruster, *Sci. Total Environ.*, 2021, **784**, 147394.

46 D. Ng, D. Acharya, X. Wang, C. D. Easton, J. Wang and Z. Xie, *J. Chem. Technol. Biotechnol.*, 2021, **96**, 2681–2695.

47 Y. Shi, H. Yi, F. Gao, S. Zhao, Z. Xie and X. Tang, *J. Hazard. Mater.*, 2021, **413**, 125361.

48 C. Zhang, T. Chen, H. Liu, D. Chen, B. Xu and C. Qing, *Appl. Surf. Sci.*, 2018, **457**, 1116–1125.

49 J. Jia, R. Ran, X. Guo, X. Wu, W. Chen and D. Weng, *Catal. Commun.*, 2019, **119**, 139–143.

50 Y. Li, Y. P. Li, P. Wang, W. Hu, S. Zhang, Q. Shi and S. Zhan, *Chem. Eng. J.*, 2017, **330**, 213–222.

51 F. Gao, X. Tang, H. Yi, S. Zhao, J. Wang and T. Gu, *Appl. Surf. Sci.*, 2019, **466**, 411–424.

52 Q. Yan, S. Chen, C. Zhang, Q. Wang and B. Louis, *Appl. Catal., B*, 2018, **238**, 236–247.

53 Y. Shi, H. Yi, F. Gao, S. Zhao, Z. Xie and X. Tang, *Sep. Purif. Technol.*, 2021, **265**, 118517.

54 Q. Zhao, B. Chen, J. Li, X. Wang, M. Crocker and C. Shi, *Appl. Catal., B*, 2020, **277**, 119215.

55 J. Huang, H. Huang, H. Jiang and L. Liu, *Catal. Today*, 2019, **332**, 49–58.

56 Z. Fan, J. Shi, C. Gao, G. Gao, B. Wang, Y. Wang, C. He and C. Niu, *Chem. Eng. J.*, 2018, **348**, 820–830.

57 C. Li, X. Tang, H. Yi, L. Wang, X. Cui, C. Chu, J. Li, R. Zhang and Q. Yu, *Appl. Surf. Sci.*, 2018, **428**, 924–932.

58 Y. Jia, J. Jiang, R. Zheng, L. Guo, J. Yuan, S. Zhang and M. Gu, *J. Hazard. Mater.*, 2021, **412**, 125258.

59 S. Li, B. Huang and C. Yu, *Catal. Commun.*, 2017, **98**, 47–51.

60 H. Chang, X. Chen, J. Li, L. Ma, C. Wang, C. Liu, J. W. Schwank and J. Hao, *Environ. Sci. Technol.*, 2013, **47**, 5294–5301.

61 D. Ren, K. Gui and S. Gu, *Appl. Surf. Sci.*, 2021, **561**, 149847.

62 S. Hao, Y. Cai, C. Sun, J. Sun, C. Tang and L. Dong, *Catalysts*, 2020, **10**, 1329.

63 F. Gao, X. Tang, H. Yi, J. Li, S. Zhao, J. Wang, C. Chu and C. Li, *Chem. Eng. J.*, 2017, **317**, 20–31.

64 Y. Liu, Y. Hou, X. Han, J. Wang, Y. Guo, N. Xiang, Y. Bai and Z. Huang, *ChemCatChem*, 2020, **12**, 953–962.

65 G. Li, D. Mao, M. Chao, G. Li, J. Yu and X. Guo, *J. Rare Earths*, 2021, **39**, 805–816.

66 A. Serrano-Lotina, M. Monte, A. Iglesias-Juez, P. Pavon-Cadierno, R. Portela and P. Avila, *Appl. Catal., B*, 2019, **256**, 117821.

67 B. Jia, J. Guo, H. Luo, S. Shu, N. Fang and J. Li, *Appl. Catal., A*, 2018, **553**, 82–90.

68 S. Raja, M. S. Alphin and L. Sivachandiran, *Catal. Sci. Technol.*, 2020, **10**, 7795–7813.

69 Z. Wu, R. Jin, Y. Liu and H. Wang, *Catal. Commun.*, 2008, **9**, 2217–2220.

70 X. Zhang, X. Zhang, X. Yang, Y. Chen, X. Hu and X. Wu, *Chem. Eng. Sci.*, 2021, **238**, 116588.

71 W. Zhao, Y. Tang, Y. Wan, L. Li, S. Yao, X. Li, J. Gu, Y. Li and J. Shi, *J. Hazard. Mater.*, 2014, **278**, 350–359.

72 X. Yao, T. Kong, S. Yu, L. Li, F. Yang and L. Dong, *Appl. Surf. Sci.*, 2017, **402**, 208–217.

73 L. Liu, B. Shen, M. Si, P. Yuan, F. Lu, H. Gao, Y. Yao, C. Liang and H. Xu, *RSC Adv.*, 2021, **11**, 18945–18959.

74 Y. Zeng, Z. Wu, L. Guo, Y. Wang, S. Zhang and Q. Zhong, *Mol. Catal.*, 2020, **488**, 110916.

75 J. Li, C. Zhang, Q. Li, T. Gao, S. Yu, P. Tan, Q. Fang and G. Chen, *Chem. Eng. Sci.*, 2022, **251**, 117438.

76 H. Yan, N. Zhang and D. Wang, *Chem Catal.*, 2022, **2**, 1594–1623.

77 L. Li, B. Sun, J. Sun, S. Yu, C. Ge, C. Tang and L. Dong, *Catal. Commun.*, 2017, **100**, 98–102.

78 X. Liu, Z. Sui, H. Chen, Y. Chen, H. Liu, P. Jiang, Z. Shen, W. S. Linghu and X. Wu, *J. Environ. Sci.*, 2021, **104**, 137–149.

79 Y. Liang, X. Wang, Q. Zhang, S. Luo and Y. Zhou, *J. Fuel Chem. Technol.*, 2020, **48**, 205–212.

80 W. Xu, G. Zhang, H. Chen, G. Zhang, Y. Han, Y. Chang and P. Gong, *Chin. J. Catal.*, 2018, **39**, 118–127.

81 S. Mohan, P. Dinesha and S. Kumar, *Chem. Eng. J.*, 2020, **384**, 123253.

82 J. Chen, W. Huang, S. Bao, W. Zhang, T. Liang, S. Zheng, L. Yi, L. Guo and X. Wu, *RSC Adv.*, 2022, **12**, 27746–27765.

83 X. Lou, P. Liu, J. Li, Z. Li and K. He, *Appl. Surf. Sci.*, 2014, **307**, 382–387.

84 G. Li, B. Wang, H. Wang, J. Ma, W. Xu, Y. Li, Y. Han and Q. Sun, *Catal. Commun.*, 2018, **108**, 82–87.

85 J. Yang, S. Ren, T. Zhang, Z. Su, H. Long, M. Kong and L. Yao, *Chem. Eng. J.*, 2020, **379**, 122398.

86 L. Yao, Q. Liu, S. Mossin, D. Nielsen, M. Kong, L. Jiang, J. Yang, S. Ren and J. Wen, *J. Hazard. Mater.*, 2020, **387**, 121704.

87 J. Jiao, S. Li and B. Huang, *Acta Phys.-Chim. Sin.*, 2015, **31**, 1383–1390.

88 Y. Zhang, Y. Chen, J. Huang, M. Ding, X. Li and H. Zhao, *Curr. Nanosci.*, 2021, **17**, 298–306.

89 J. Yang, J. Zhou, W. Tong, T. Zhang, M. Kong and S. Ren, *J. Energy Inst.*, 2019, **92**, 1158–1166.

90 S. He, Q. Li, Q. Zhang, Z. Zhan and L. Wang, *J. Environ. Eng.*, 2019, **145**, 04019087.

91 Y. Qi, X. Shan, M. Wang, D. Hu, Y. Song, P. Ge and J. Wu, *Water Air Soil Pollut.*, 2020, **231**, 289.

92 S. Ding, C. Li, J. Zhang, J. Wu, Y. Yue and G. Qian, *Appl. Surf. Sci.*, 2022, **595**, 153484.

93 Z. Yang, P. Tang, C. Xu, B. Zhu, Y. He, T. Duan, J. He, G. Zhang and P. Cui, *J. Energy Inst.*, 2023, **108**, 101201.

94 J. Li, L. Shi, S. Lyu, X. Yang, X. Yan and X. Zhang, *Environ. Chem.*, 2023, **42**, 3568–3578.

95 H. Zhao, H. Wang and Z. Qu, *J. Environ. Sci.*, 2022, **112**, 231–243.

96 Z. Cai, Y. Yang, Z. Feng, J. Zhang, Y. Yue and G. Qian, *Colloids Surf., A*, 2024, **683**, 133079.

97 S. Zhao, K. Song, R. Jiang, D. Ma, H. Long and J. Shi, *Catal. Today*, 2023, **423**, 113966.

98 W. Xie, G. Zhou, X. Zhang, J. Zhang, G. Zhang and Z. Tang, *Mol. Catal.*, 2020, **34**, 546–558.

99 Y. Li, P. Jiang, J. Tian, Y. Liu, Y. Wan, K. Zhang, D. Wang, J. Dan, B. Dai, X. Wang and F. Yu, *J. Environ. Chem. Eng.*, 2021, **9**, 105753.

100 X. Zhang, S. Lv, X. Zhang, K. Xiao and X. Wu, *J. Environ. Sci.*, 2021, **101**, 1–15.

101 J. Gu, R. Duan, W. Chen, Y. Chen, L. Liu and X. D. Wang, *Catalysts*, 2020, **10**, 566.

102 Z. Guo, W. Huo, Y. Zhang, S. Ren and J. Yang, *Mater. Herald*, 2021, **35**, 13085–13099.

103 L. Lietti, J. L. Alemany, P. Forzatti, G. Busca, G. Ramis, E. Giamello and F. Bregani, *Catal. Today*, 1996, **29**, 143–148.

104 C. Tang, H. Zhang and L. Dong, *Catal. Sci. Technol.*, 2016, **6**, 1248–1264.

105 S. Yang, C. Wang, J. Li, N. Yan, L. Ma and H. Chang, *Appl. Catal., B*, 2011, **110**, 71–80.

106 T. Chen, B. Guan, H. Lin and L. Zhu, *Chin. J. Catal.*, 2014, **35**, 294–301.

107 X. Li, Q. Li, L. Zhong, Z. Song, S. Yu, C. Zhang, Q. Fang and G. Chen, *J. Phys. Chem. C*, 2019, **123**, 25185–25196.

108 Z. Fei, Y. Yang, M. Wang, Z. Tao, Q. Liu, X. Chen, M. Cui, Z. Zhang, J. Tang and X. Qiao, *Chem. Eng. J.*, 2018, **353**, 930–939.

109 G. Ramis, L. Yi, G. Busca, M. Turco, E. Kotur and R. J. Willey, *J. Catal.*, 1995, **157**, 523–535.

110 G. Qi, R. Yang and R. Chang, *Appl. Catal., B*, 2004, **51**, 93–106.

111 P. Sun, R. Guo, S. Liu, S. Wang, W. Pan and M. Li, *Appl. Catal., A*, 2017, **531**, 129–138.

112 N. Fang, J. Guo, S. Shu, H. Luo, J. Li and Y. Chu, *J. Taiwan Inst. Chem. Eng.*, 2018, **93**, 277–288.

113 S. Gu, K. Gui, D. Ren and Y. Wei, *React. Kinet. Mech. Catal.*, 2020, **130**, 741–751.

114 F. Wang, S. D. Li, R. Y. You, Z. K. Han, W. T. Yuan, B. E. Zhu, Y. Gao, H. S. Yang and Y. Wang, *Appl. Surf. Sci.*, 2023, **638**, 158124.

115 G. Li, B. Wang, Z. Wang, Z. Li, Q. Sun, W. Q. Xu and Y. Li, *J. Phys. Chem. C*, 2018, **122**, 20210–20231.

116 S. Yang, S. Xiong, Y. Liao, X. Xiao, F. Qi, Y. Peng, Y. Fu, W. Shan and J. Li, *Environ. Sci. Technol.*, 2014, **48**, 10354–10362.

117 S. Yang, Y. Fu, Y. Liao, S. Xiong, Z. Qu, N. Yan and J. Li, *Catal. Sci. Technol.*, 2014, **4**, 224–232.

118 L. Zhang, X. Wen, Z. Lei, L. Gao, X. Sha, Z. Ma, H. He, Y. Wang, Y. Jia and Y. H. Li, *AIP Adv.*, 2018, **8**, 045004.

119 C. Yu, L. Wang and B. Huang, *Aerosol Air Qual. Res.*, 2015, **15**, 1017–1027.

120 Y. Huo, K. Liu, J. Liu and H. He, *Appl. Catal., B*, 2022, **301**, 120784.

121 J. Tang, X. Wang, H. Li, L. Xing and M. Liu, *ACS Omega*, 2023, **8**, 7262–7278.

122 G. Xu, X. Guo, X. Cheng, J. Yu and B. Fang, *Nanoscale*, 2021, **13**, 7052–7080.

123 Y. Liu, J. Liu, B. Zhu, J. Chen, F. Li and Y. Sun, *Colloids Surf., A*, 2023, **662**, 130983.

124 D. An, J. Ji, Q. Cheng, X. Zhao, Y. Cai, W. Tan, Q. Tong, K. Ma, W. Zou, J. Sun, C. Tang and L. Dong, *Environ. Sci. Technol.*, 2023, **57**, 14737–14746.

125 S. Xiong, Y. Liao, X. Xiao, H. Dang and S. Yang, *Catal. Sci. Technol.*, 2015, **5**, 2132–2140.

126 D. Yan, X. Hong, J. Li, Y. Wang, Y. Pan and H. Gong, *J. Phys. Chem. Solids*, 2024, **192**, 112703.

127 L. Lin, T. Hsieh, J. Hsu and Y. Wang, *Appl. Surf. Sci.*, 2023, **614**, 156139.

128 C. Hu, C. Liu, K. Du, C. Pang, Z. Zhuo and Q. Gao, *J. Environ. Chem. Eng.*, 2023, **11**, 110440.

129 X. Yao, T. Kong, S. Yu, L. Li, F. Yang and L. Dong, *Appl. Surf. Sci.*, 2017, **402**, 208–217.

130 F. Liu and H. He, *Catal. Today*, 2010, **153**, 70–76.

131 R. Guo, B. Qin, L. Wei, T. Yin, J. Zhou and W. Pan, *Phys. Chem. Chem. Phys.*, 2022, **24**, 6363–6382.

132 S. Liu, Y. Ji, W. Xu, J. Zhang, R. Jiang, L. Li, L. Jia, Z. Zhong, G. Xu, T. Zhu and F. Su, *J. Catal.*, 2022, **406**, 72–86.

133 Y. Pan, N. Li, S. Ran, D. Wen, Q. Luo, K. Li and Q. Zhou, *Ind. Eng. Chem. Res.*, 2022, **61**, 9991–10003.

134 L. Wang, X. Cheng, Z. Wang, C. Ma and Y. Qin, *Appl. Catal., B*, 2017, **201**, 636–651.

135 P. Zang, J. Liu, G. Zhang, B. Jia, Y. He, Y. Wang and Y. Lv, *Fuel*, 2023, **331**, 125800.

136 C. Sun, W. Chen, X. Jia, A. Liu, F. Gao, S. Feng and L. Dong, *Chin. J. Catal.*, 2021, **42**, 417–430.

137 Y. Wang, W. Yi, Y. Zeng and H. Chang, *Environ. Sci. Technol.*, 2020, **54**, 12612–12620.

138 L. Han, M. Gao, J. Hasegawa, S. Li, Y. Shen, H. Li, L. Shi and D. Zhang, *Environ. Sci. Technol.*, 2019, **53**, 6462–6473.

139 X. Zhang, S. Liu, K. Ma, Y. Chen, S. Jin, X. Wang and X. Wu, *Catalysts*, 2021, **11**, 1360.

140 G. Xiao, Z. Guo, J. Li, Y. Du, Y. Zhang, T. Xiong, B. Lin, M. Fu, D. Ye and Y. Hu, *Chem. Eng. J.*, 2022, **435**, 134914.

141 W. Jiang, W. Yu, F. Bi, P. Sun, X. Weng and Z. Wu, *Environ. Sci. Technol.*, 2019, **53**, 12657–12667.

142 S. Xiong, Y. Peng, D. Wang, N. Huang, Q. Zhang, S. Yang, J. Chen and J. Li, *Chem. Eng. J.*, 2020, **387**, 124090.

143 R. Chen, X. Fang, J. Li, Y. Zhang and Z. Liu, *Chem. Eng. J.*, 2023, **452**, 139207.

144 X. Shi, J. Guo, T. Shen, A. Fan, S. Yuan and J. Li, *Chem. Eng. J.*, 2021, **421**, 129995.

145 W. Yoon, Y. Kim, G. J. Kim, J. R. Kim, S. J. Lee, H. Y. S. Han, G. H. Park, H. J. Chae and W. B. Kim, *Chem. Eng. J.*, 2022, **434**, 134676.

146 D. Yan, J. Zhao, J. Li, G. Abbas, Z. Chen and T. Guo, *Catal. Lett.*, 2023, **153**, 2838–2852.

147 G. Yao, Y. Wei, K. Gui and X. Ling, *J. Environ. Sci.*, 2022, **115**, 126–139.

148 D. Damma, D. K. Pappas, T. Boningari and P. G. Smirniotis, *Appl. Catal., B*, 2021, **287**, 119939.

149 X. Jia, H. Liu, Y. Zhang, W. Chen, Q. Tong, G. Piao, C. Sun and L. Dong, *J. Colloid Interface Sci.*, 2021, **581**, 427–441.

150 H. Wang, B. Huang, C. Yu, M. Lu, H. Huang and Y. Zhou, *Appl. Catal., A*, 2019, **588**, 117207.

151 K. H. P. Reddy, B. S. Kim, S. S. Lam, S. C. Jung, J. Song and Y. K. Park, *Environ. Res.*, 2021, **195**, 110876.

152 H. W. Ryu, M. Y. Song, J. S. Park, J. M. Kim, S. C. Jung, J. Song, B. J. Kim and Y. K. Park, *Environ. Res.*, 2019, **172**, 649–657.

153 D. Wang, Q. Yao, S. Liu, S. Hui and Y. Niu, *J. Energy Inst.*, 2019, **92**, 1852–1863.

154 I. Song, H. Lee, S. W. Jeon and D. Kim, *ACS Catal.*, 2020, **10**, 12017–12030.

155 R. Cui, X. Huang, G. Zhang and Z. Tang, *Ind. Eng. Chem. Res.*, 2024, **63**, 7003–7017.

156 B. Qin, R. Guo, J. Zhou, L. Wei, T. Yin and W. Pan, *Appl. Surf. Sci.*, 2022, **598**, 153823.

157 L. Wei, R. Guo, J. Zhou, B. Qin, X. Chen, Z. Bi and W. Pan, *Fuel*, 2022, **316**, 123438.